

RESEARCH ARTICLE | MAY 12 2025

Bio-inspired adaptive flexible tube wave energy converters: Resonant fluid–structure interaction and power extraction ^{EP}



Yang Huang (黄扬) ^{ORCID}; Qing Xiao (肖清) ^{ORCID} ✉; Guillermo Idarraga ^{ORCID}; Liu Yang (杨柳) ^{ORCID}; Saishuai Dai (戴赛帅) ^{ORCID}; Farhad Abad ^{ORCID}; Feargal Brennan ^{ORCID}; Saeid Lotfian ^{ORCID}

Check for updates

Physics of Fluids 37, 053104 (2025)

<https://doi.org/10.1063/5.0270834>



Articles You May Be Interested In

Two-scale structure of the current layer controlled by meandering motion during steady-state collisionless driven reconnection

Phys. Plasmas (July 2004)



Physics of Fluids
Special Topics
Open for Submissions

[Learn More](#)



Bio-inspired adaptive flexible tube wave energy converters: Resonant fluid–structure interaction and power extraction

Cite as: Phys. Fluids **37**, 053104 (2025); doi: [10.1063/5.0270834](https://doi.org/10.1063/5.0270834)

Submitted: 13 March 2025 · Accepted: 17 April 2025 ·

Published Online: 12 May 2025



View Online



Export Citation



CrossMark

Yang Huang (黄扬),¹  Qing Xiao (肖清),^{1,a)}  Guillermo Idarraga,²  Liu Yang (杨柳),²  Saishuai Dai (戴赛帅),¹ 
Farhad Abad,¹  Feargal Brennan,¹  and Saeid Lotfian¹ 

AFFILIATIONS

¹Department of Naval Architecture, Ocean & Marine Engineering, University of Strathclyde, Glasgow G4 0LZ, United Kingdom

²Advanced Composite Group, Department of Mechanical and Aerospace Engineering, University of Strathclyde, Glasgow G1 1XJ, United Kingdom

Note: This paper is part of the Special Topic, Wave-Structure Interaction.

^{a)} Author to whom correspondence should be addressed: qing.xiao@strath.ac.uk

ABSTRACT

Flexible tube wave energy converters (WECs) are a novel class of devices utilizing deformable materials, offering structural simplicity, broadband energy conversion, and adaptability to diverse wave conditions. While prior studies have examined their hydro-elastic behavior, the nonlinear coupling between internal and external fluid fields and its impact on fluid–structure interaction (FSI) responses remain insufficiently understood. This study employs a high-fidelity FSI framework, integrating computational fluid dynamics and finite element analysis, to investigate the dynamic performance of two flexible WEC designs: S3 and Anaconda. Numerical simulations across varying wave conditions reveal distinct dynamic features. The S3 WEC supports multiple internal standing wave modes, enabling broadband resonant energy harvesting, whereas the Anaconda exhibits resonance at a single dominant frequency. Internal fluid flows in both devices show complex three-dimensional motions, challenging conventional one-dimensional flow assumptions. Structural stress distributions also differ, with peak stresses in the S3 aligning with the anti-nodes of internal standing waves, while in the Anaconda, they concentrate near the stern. These findings enhance the understanding of coupled fluid–structure dynamics in flexible WECs and offer theoretical guidance for their design optimization and deployment in real-sea environments.

© 2025 Author(s). All article content, except where otherwise noted, is licensed under a Creative Commons Attribution (CC BY) license (<https://creativecommons.org/licenses/by/4.0/>). <https://doi.org/10.1063/5.0270834>

I. INTRODUCTION

Among various ocean renewable energy technologies, wave energy converters (WECs) have long been regarded as a promising means of harvesting vast ocean energy resources. However, conventional rigid-body WECs face significant challenges, including high manufacturing and maintenance costs, structural fatigue under harsh sea conditions, and limited adaptability to varying wave environments, which hinder their commercial viability.^{1–3}

Inspired by the adaptive deformation observed in marine organisms, researchers have explored alternative WEC designs that leverage flexible materials to improve energy conversion efficiency, structural durability, and operational adaptability. This has led to the development of flexible wave energy converters (FlexWECs), which integrate flexible materials into both their primary energy-absorbing structures

and Power Take-Off (PTO) systems to achieve enhanced performance.⁴ Various FlexWEC designs have been proposed, including flexible oscillating water column (OWC) WECs, pneumatic cell based FlexWECs, and flexible tube WECs.⁵

Among these, flexible tube WECs take inspiration from elongated marine organisms, such as sea snakes and eels, which utilize body undulations to efficiently interact with surrounding flows. These WECs feature a long, submerged, pressurized flexible tube that aligns parallel to incoming waves. As waves propagate over the tube, the resulting pressure difference across the tube's wall generates traveling deformations known as “bulge wave.” This phenomenon further induces cyclic expansions and contractions of the tube's cross section, leading to variations in internal hydraulic pressure. The energy captured in this process is subsequently converted into internal fluid energy, which

is then extracted and transformed into electrical power using either mechanical turbine-based systems or dielectric elastomer generator (DEG)-based PTO systems.

Currently, two prominent flexible tube WEC designs based on the bulge wave principle are the Anaconda and the S3, as shown in Fig. 1.

- The Anaconda WEC, first patented by Farley and Rainey in 2006, is under development and testing by Checkmate Flexible Engineering Ltd.^{6,7} This design relies on a single PTO located at the tube's stern, where the bulge wave energy is ultimately extracted using a mechanical turbine-based system. The flexible tube acts primarily as a passive energy harvester, converting wave-induced bulge wave energy into fluid kinematic energy.
- The S3, introduced by SBM Offshore in 2009,^{1,8} incorporates multiple PTOs distributed along the tube's length, each based on dielectric elastomer generators (DEGs). In this configuration, the flexible tube serves as both the primary energy absorber and the PTO mechanism, directly converting mechanical deformation into electrical energy.

Both WECs share an elongated, flexible structure but differ in their internal energy conversion mechanisms and power extraction methodologies. These distinctions influence their hydrodynamic behavior, particularly under resonant conditions, which will be thoroughly analyzed in Secs. III–V.

To advance the commercialization of flexible tube WECs, several physical model experiments^{1,9–14} and numerical analysis^{15–17} have been conducted.

The Anaconda WEC has undergone several laboratory-scale hydrodynamic tests, focusing on hydrodynamic responses, PTO efficiency, and fluid–structure interactions (FSIs). Early experiments by Chaplin *et al.*^{9,15} demonstrated that the WEC can achieve substantial energy capture across a range of wave frequencies. Heller *et al.*¹⁰ further investigated wave radiation effects using a scaled model, while subsequent studies^{11,16} explored the role of PTO impedance on energy extraction efficiency. Mendes *et al.*^{12,13} analyzed air-compressibility effects and scale-dependent power output variations through additional wave tank experiments. Yu *et al.*¹⁴ investigated the effects of relative hydraulic head and tube length on the system's hydrodynamic efficiency through experimental testing.

The S3 WEC, in contrast, has received less experimental attention. The pioneering work by Jean *et al.*¹ demonstrated the first successful wave-to-electricity conversion using a submerged electroactive polymer (EAP) WEC under laboratory wave conditions. Later studies, such as Babarit *et al.*,¹⁷ developed a linearized numerical model based

on potential flow theory and linearized wall equations to predict hydro-elastic behavior, particularly standing wave formation within the flexible tube.

Although the above-mentioned studies capture the main features of flexible tube WECs, due to the nature of existing methodologies, a deep understanding of the detailed fluid-flexible structure–interaction phenomena, especially the complex fluid flow inside the deformable tube and the distributed stress along the tube, is limited. For instance, the reduced-order models adopted in previous theoretical analysis often simplify flow field resolution and structural computations, failing to capture nonlinear response characteristics and flow field evolution accurately.

To address these limitations, high-fidelity Computational Fluid Dynamics (CFD)-Finite Element Analysis (FEA) approaches have been introduced to simulate fluid–structure interaction (FSI) dynamics in FlexWEC systems. Previous applications of CFD-FEA frameworks in wave energy studies include the Bombora WEC¹⁸ and Variable Shape Buoy (VSB) WECs.^{19,20} However, applications of such high-fidelity models to flexible tube WECs remain unexplored, due to high computational costs, instabilities in FSI interface motion, nonlinear behavior of flexible materials, and complex coupling strategies. While similar research exists in biofluid mechanics (e.g., blood vessel simulations),^{21–26} flexible tube WECs fall outside their scopes.

This study forms a key component of the “Bionic Adaptive Stretchable Materials for Wave Energy Converters” research project.²⁷ Drawing inspiration from aquatic animals, the project seeks to develop innovative, flexible material-based wave energy converters and has already provided significant insight into the performance of flexible materials and OWC WECs.^{28–32} Building on this foundation, the present work aims to enhance the understanding of FSI responses in flexible tube-shape WECs, particularly the complex internal and external flow field characteristics. An advanced FSI analysis tool²⁹ based on a CFD-FEA approach is employed to conduct numerical simulations for the Anaconda and S3 WECs under regular wave conditions at various frequencies. The results provide a comprehensive analysis of resonant responses, flow field details, structural responses, and power output. Additionally, a comparative study of the FSI responses of the Anaconda and S3 WECs is presented.

The structure of this paper is organized as follows: Section II introduces the FSI analysis tool. Sections III and IV present numerical results and in-depth analysis of the FSI responses of the S3 and Anaconda WECs, respectively. Sections V and VI discuss the insights obtained and provide concluding remarks.

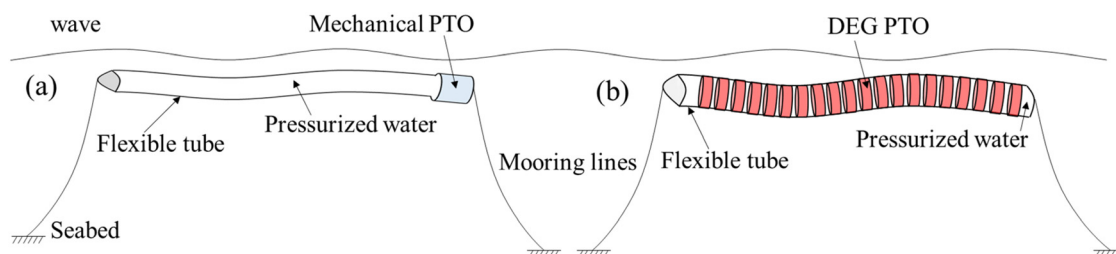


FIG. 1. Schematic diagram of flexible tube WECs: (a) Anaconda and (b) S3.

II. NUMERICAL METHOD

An FSI analysis tool integrating Open FOAM, CalculiX, and preCICE was established in our previous work.^{30–32} Using this tool, we have addressed various FSI problems, including a three-dimensional (3D) flexible plate in uniform current, an elastic disk, a flexible OWC WEC, and a preliminary study of flexible tube WEC with regular waves. The results, validated against experimental data and other numerical findings, demonstrate the reliability and accuracy of the tool.³⁰ In the present study, we further extend the tool to enable coupled simulations of the internal flow field, external flow field, and structural field and employed it to perform numerical simulations of the S3 and Anaconda WECs under various wave conditions. A brief overview of the numerical methods is provided in this section.

A. Fluid modeling

A CFD solver developed based on Open FOAM is adopted to simulate the two-phase incompressible viscous flows around the flexible tube WECs.^{33,34} The governing equations include continuity equations and momentum equations, which are defined as follows:

$$\nabla \cdot \mathbf{u} = 0, \quad (1)$$

$$\frac{\partial(\rho\mathbf{u})}{\partial t} + \nabla \cdot (\rho(\mathbf{u} - \mathbf{u}_g))\mathbf{u} = -\nabla p_d - \mathbf{g} \cdot x\nabla\rho + \nabla \cdot (\mu\nabla\mathbf{u}) + (\nabla\mathbf{u}) \cdot \nabla\mu + f_\sigma + f_p, \quad (2)$$

where \mathbf{u} represents the flow velocity, ρ denotes the mixture density of the air and water phases, \mathbf{u}_g is the velocity of mesh grid, induced by the mesh deformation, p_d is the dynamic pressure, \mathbf{g} is the gravity acceleration, μ is the dynamic viscosity, f_σ is the surface tension term, and f_p is the source term generated by the porous media, representing the PTO.

The fluid solver employs the finite volume method (FVM) to discretize the governing equations in the fluid domain. The volume of fluid (VOF) method is used to capture the free surface. Stoke II wave theory is used to calculate the incident wave velocity and elevation. Active wave absorption technique is applied to estimate the effect of wave reflection.^{33,34} Laminar flow is utilized for low Reynolds number flows in subsequent simulations. Additionally, mooring lines attached to the floating structure are simplified as springs. For dynamic mesh handling, a moving-mesh technique is employed, based on solving a Laplace equation with variable mesh point diffusivity to manage mesh deformation resulting from the FSI interface, as formulated in the following equation:

$$\nabla \cdot (\gamma\nabla X_g) = 0, \quad \gamma = \frac{1}{r^2}, \quad (3)$$

where X_g is the displacement of mesh points obtained from the structural deformation and γ denotes the diffusivity field, which varies quadratically with the inverse of the distance r between the cell center and the deformed interface.

B. Structure modeling

A three-dimensional (3D) finite element method (FEM) code is employed to predict the structural dynamics of the flexible tube.³⁵ This code inherently accounts for the geometric nonlinearity of the structure, and material nonlinearity is also addressed by employing

hyper-elastic material models. The weak form of the balance of momentum is adopted as the governing equation, which can be written as follows:

$$\rho_s \frac{D\mathbf{v}}{Dt} = \nabla \cdot \mathbf{S} + \mathbf{f}_b, \quad (4)$$

where ρ_s denotes the density of structure, \mathbf{v} is the velocity of material point, \mathbf{S} represents stress tensor, and \mathbf{f}_b is the body force vector.

Based on the finite element method, the governing equations are discretized into the following algebraic equation system:

$$[\mathbf{M}]\{\mathbf{a}\} + [\mathbf{C}]\{\mathbf{v}\} + [\mathbf{K}]\{\mathbf{x}\} = \{\mathbf{f}\}, \quad (5)$$

where $[\mathbf{M}]$, $[\mathbf{C}]$, and $[\mathbf{K}]$ are the global mass, damping, and stiffness matrices, respectively; $\{\mathbf{x}\}$, $\{\mathbf{v}\}$, and $\{\mathbf{a}\}$ denote the displacement, velocity, and acceleration vectors, respectively; and $\{\mathbf{f}\}$ represents the global force vector. Additionally, the α -method is employed to discretize the governing equations in time domain.

C. Fluid-structure coupling

A partitioned coupling strategy is employed for strong coupling between the fluid and solid domains.³⁶ In this framework, the fluid solver computes the flow field while the structural solver handles the deformation of the structure. To enable effective data transfer between solvers using different meshes, radial basis function (RBF) interpolation is utilized for exchanging forces and displacements.³⁷ Convergence is assessed by computing the discrete l_2 norm of the difference between solutions from successive iterations. The computation proceeds to the next time step once the l_2 norm meets the specified convergence criterion or when the maximum iteration number (k_N) is reached. A schematic of the simplified sub-iteration loop for the FSI coupling is presented in Fig. 2. Additionally, an improved interface-quasi-Newton with inverse Jacobian from a least squares model (IQN-ILS)³⁸ is used to accelerate the coupling iterations of FSI simulations.

To simulate the coupled interactions among the internal flow, external flow, and structural fields in the S3 WEC, the FSI framework is expanded to integrate these 3 distinct physical domains while maintaining the partitioned coupling strategy. As depicted in Fig. 3, the numerical simulation of the S3 WEC is divided into three distinct domains: the internal flow field, the external flow field, and the structural field. The internal flow field, representing the incompressible fluid within the fully enclosed tube, is modeled using a single-phase flow model since the tube remains filled with pressurized water. In contrast, the external flow field, which simulates the fluid motion surrounding the tube and incorporates incident waves and free-surface effects, is computed using a two-phase flow model. The structural field captures both the local deformation and the global motion of the slender, thin-walled tube. Each domain is independently modeled and meshed, with data exchanged at the FSI interfaces: the internal and external flow solvers transfer fluid forces to the tube's inner and outer surfaces, respectively, while the structural solver provides the corresponding displacement data. This bidirectional, strong coupling strategy enables the accurate prediction of the S3 WEC's hydro-elastic responses under wave conditions.

III. S3 WEC MODELING

A. Physical model

In this study, the S3 model references the work of Jean *et al.*¹ and Bararit *et al.*¹⁷ However, due to the limitations of the FSI analysis

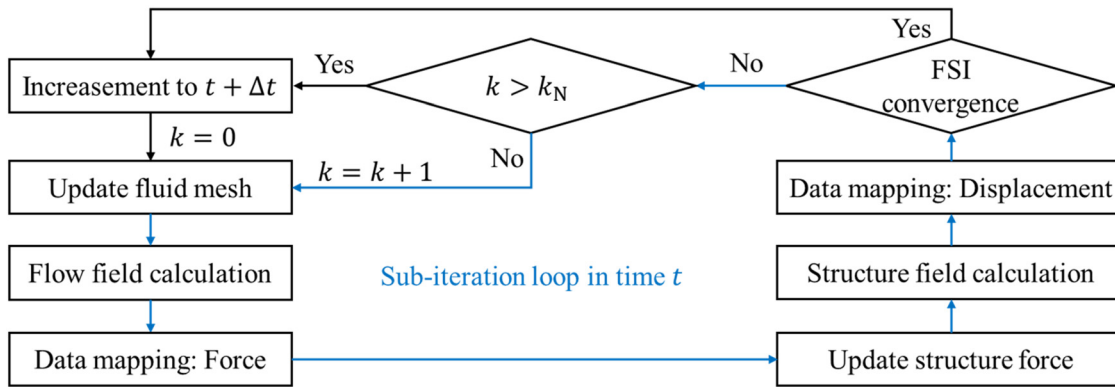


FIG. 2. Schematic diagram of sub-iteration loop of FSI coupling.

tool,³⁰ a shorter flexible tube is employed to ensure numerical convergence and stability in the simulations.

As illustrated in Fig. 4, the S3 model is positioned near the free surface and comprises rigid bow and stern sections connected by a flexible tube. The tube is made of natural rubber, and its stress-strain behavior under relatively small deformations is described using a linear elastic model, based on previous studies.^{11,13,39} Both ends of the tube are sealed and internally pressurized with water, inducing pre-stretching. The tube is anchored at both ends by two mooring lines, allowing for six-degree-of-freedom (6DoF) motion in response to incident waves. In the numerical simulation, the mooring lines are simplified as springs. The key physical parameters of the S3 model and material properties are summarized in Table I.

B. Computational setup

As shown in Fig. 5, a hexahedral computational domain is constructed with dimensions of 6.5 m (length) × 2 m (width) × 6 m (height). The S3 model is centrally positioned within this domain, submerged 0.15 m below the free surface and equidistant (1.5 m) from both the inlet and outlet. The water depth is set to 5 m. Given the relatively short distances between the model and the inlet/outlet boundaries, active wave absorption techniques are implemented to directly

dissipate reflected waves.⁴⁰ This approach eliminates the need for an excessively large computational domain, significantly reducing the computational cost of the CFD simulations.

To improve data mapping accuracy in the FSI simulations, a structured mesh is employed, with local grid refinement around the tube to enhance the resolution of its motion responses. The minimum mesh size on the tube’s surface is set to 0.042 m (x) × 0.014 m (y) × 0.014 m (z), resulting in ~1.35 × 10⁶ fluid grid elements. For the solid domain, 6558 elements are used to compute the structural deformation of the tube.

The boundary conditions are defined as follows: At the inlet, the velocity is prescribed based on the incident wave parameters. Zero-gradient conditions are applied at the outlet, front, and back boundaries, while the top boundary is defined as a pressure outlet and a no-slip condition is imposed at the bottom boundary.

To capture the standing wave modes inside the tube, a range of wave conditions is considered in the simulations, as detailed in Table II. A geometric scaling ratio of 1:30 between the numerical model and the full-scale device is adopted in this study. To ensure dynamic similarity between the model and full-scale conditions, the Froude scaling law is employed, which is widely used in wave-structure interaction problems where gravity is the dominant restoring force. The Froude number is defined as

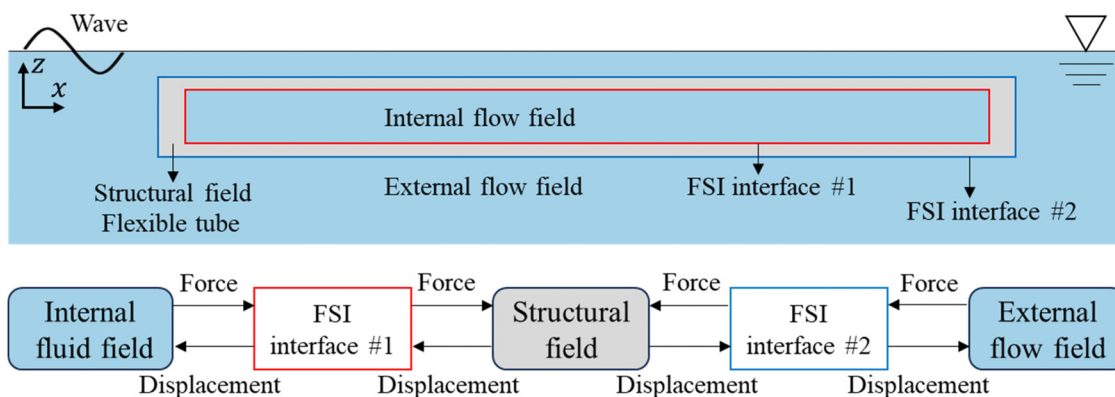


FIG. 3. Partitioned coupling strategy for the FSI simulation of the S3 WEC.

12 May 2025 11:42:06

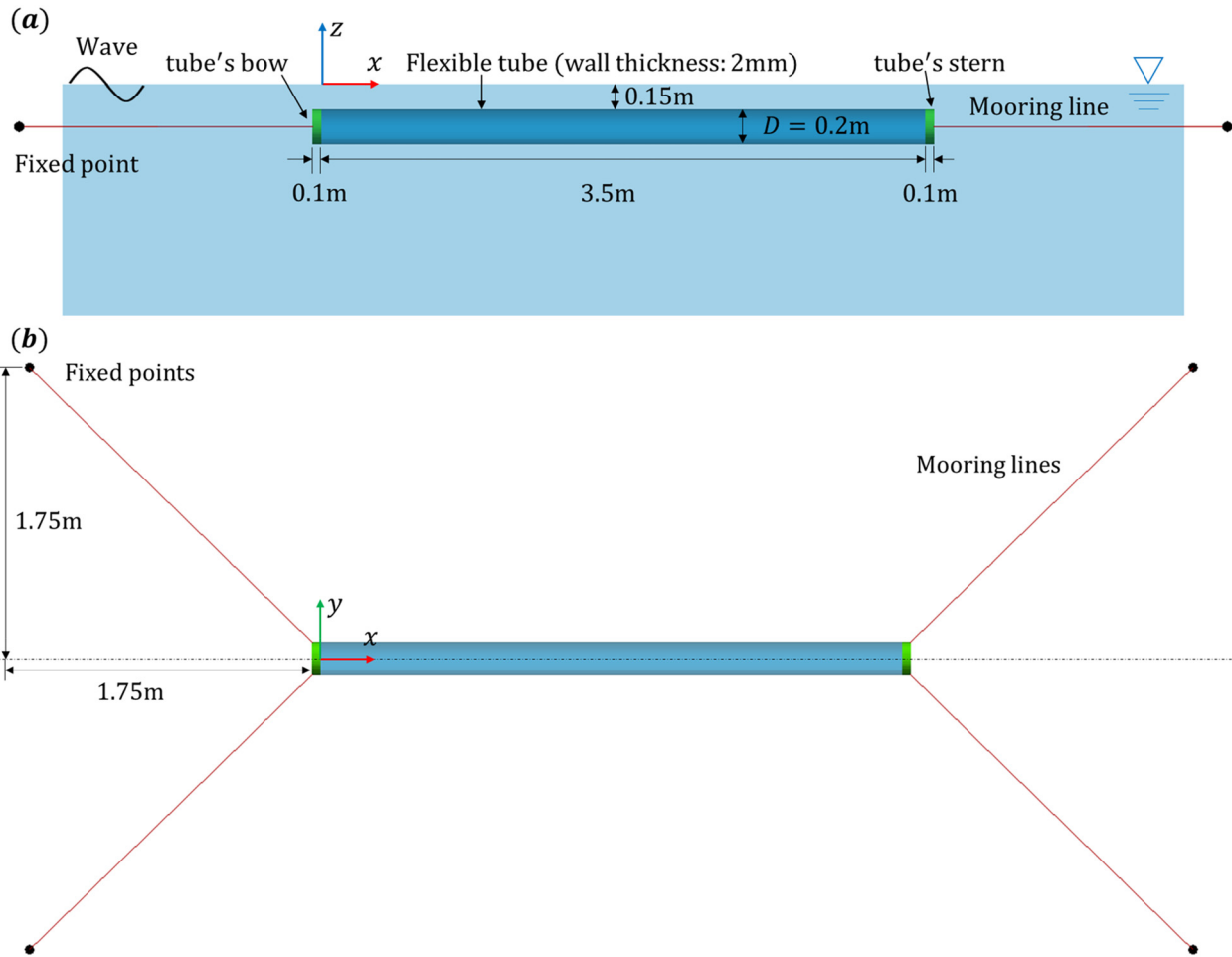


FIG. 4. Schematic diagram of the S3 WEC: (a) front view and (b) top view.

$$Fr = U_c / \sqrt{gL_c}, \tag{6}$$

where U_c is a characteristic velocity and L_c is the characteristic length. Accordingly, the wave conditions used in the simulations correspond to full-scale wave periods ranging from 4.9 to 13.4 s, which are representative of typical ocean wave environments.

C. Grid convergence test

To determine an appropriate grid resolution, a grid convergence test is conducted using three mesh configurations: coarse, medium, and fine. The minimum grid sizes on the tube surface and the total number of grid elements for each case are summarized in Table III. A regular wave with an amplitude of 0.08 m (A_w) and a period of 1.5 s (T_w) is selected for the test. The time step size is set to $2 \times 10^{-3} T_w$, ensuring that the Courant–Friedrichs–Lewy (CFL) number remains below 1. Based on prior studies, this time step is sufficiently small to prevent numerical artifacts from affecting the simulation results.^{30,31}

Figure 6 presents the time history of the heave displacement at the tube’s bow and the cross-sectional area at $x/L_t = 0.5$ under

TABLE I. Physical properties of the S3 model.

Name	Symbol	Value	Unit
Tube length	L_t	3.5	m
Tube thickness	t_0	2×10^{-3}	m
Initial inner diameter	D_0	0.2	m
Static pressure	p_s	8.2	kPa
Pre-stretched inner diameter	D_1	0.253	m
Mooring stiffness	k_m	100	N/m
Mooring pretension	f_m	57.7	N
Flexible tube density	ρ_t	960	kg/m ³
Tube ends’ density	ρ_e	1025	kg/m ³
Natural rubber: Young’s modulus	E_N	0.75	MPa
Natural rubber: Poisson’s ratio	ν_N	0.49	...

12 May 2025 11:42:06

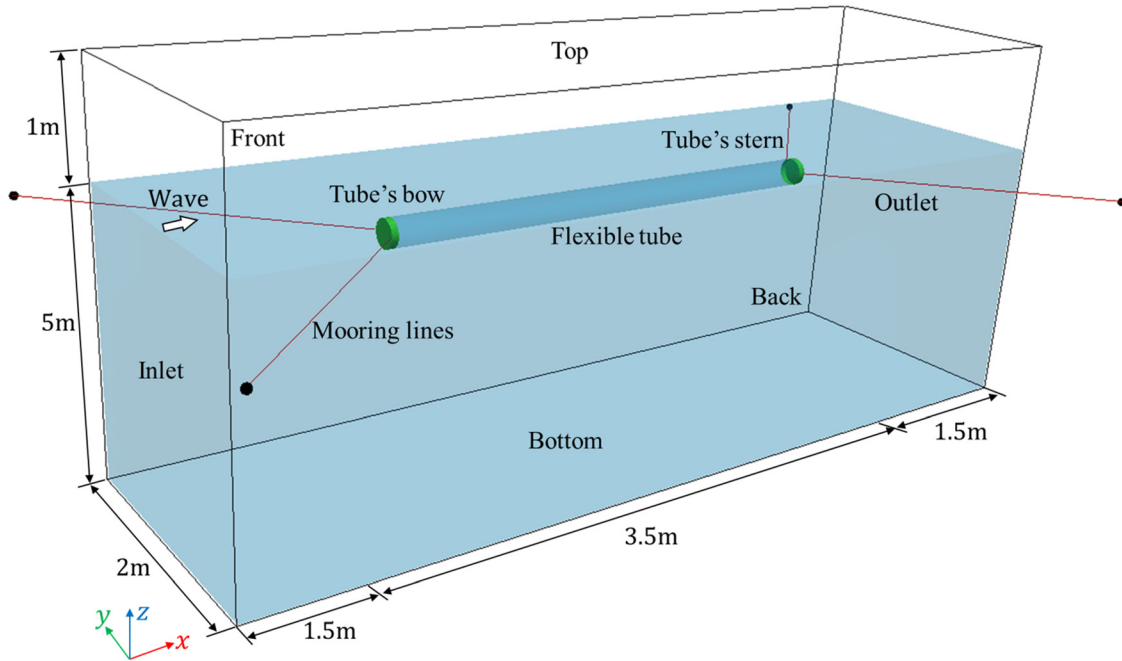


FIG. 5. Computational domain for the S3 WEC modeling.

TABLE II. Wave conditions for the S3 WEC modeling.

Wave frequency f_w (Hz)	Wave speed C_w (m/s)	Wave amplitude A_w (m)	Wavelength λ_w (m)
0.41–1.11	1.41–3.80	0.08	1.26–9.27

different mesh resolutions. The results show that the heave displacement and tube deformation obtained using the medium mesh closely match those from the fine mesh, with discrepancies of less than 3%. Therefore, the medium mesh with a time step of $2 \times 10^{-3} T_w$ is selected for the subsequent numerical simulations.

D. Resonant responses

1. Resonant conditions

A key characteristic of the S3 WEC’s resonant response is the formation of standing waves of pressure within the flexible tube. This phenomenon induces periodic radial contractions and expansions along the tube’s length, resulting in a standing wave pattern in its cross-sectional area, as illustrated in Fig. 7.

TABLE III. Mesh Information for the grid independence study of the S3 WEC model.

Mesh type	Grid size (m)	Total grid number ($\times 10^6$)
Coarse mesh	0.056 (x) \times 0.018 (y) \times 0.018 (z)	0.75
Medium mesh	0.042 (x) \times 0.014 (y) \times 0.014 (z)	1.35
Fine mesh	0.030 (x) \times 0.010 (y) \times 0.010 (z)	2.41

To understand the conditions for standing wave formation in the S3, an analogy is drawn with the Rubens tube, a classical device used to visualize standing sound waves in a cylindrical enclosure.⁴¹ The S3 bears a resemblance to the Rubens tube, wherein the sound waves of the Rubens apparatus are supplanted by oceanic pressure waves, and the flammable gas is substituted with water. In the Rubens tube, the resonant frequency (f_r) and wavelength (λ_s) of standing waves are expressed as

$$f_r = \frac{nc}{2L_t}, \quad \lambda_s = \frac{c}{f_r}, \tag{7}$$

where c is the speed of sound waves, n is a positive integer, and L_t is the tube length. However, the dynamics in the S3 WEC are more complex. Unlike the fixed ends of a Rubens tube, both ends of the S3 are moored, allowing 6DoF motion. This motion alters the distribution of internal pressure waves and affects the formation of standing waves.

To analyze the standing waves in the S3’s flexible tube, Chaplin *et al.*¹¹ developed a reduced-order model to characterize the internal flow, which can be decomposed into three traveling wave components:

- (a) A forward-traveling pressure wave at bulge wave speed,
- (b) A backward-traveling pressure wave at bulge wave speed,
- (c) A forward-traveling pressure wave at external water wave speed.

12 May 2025 11:42:06

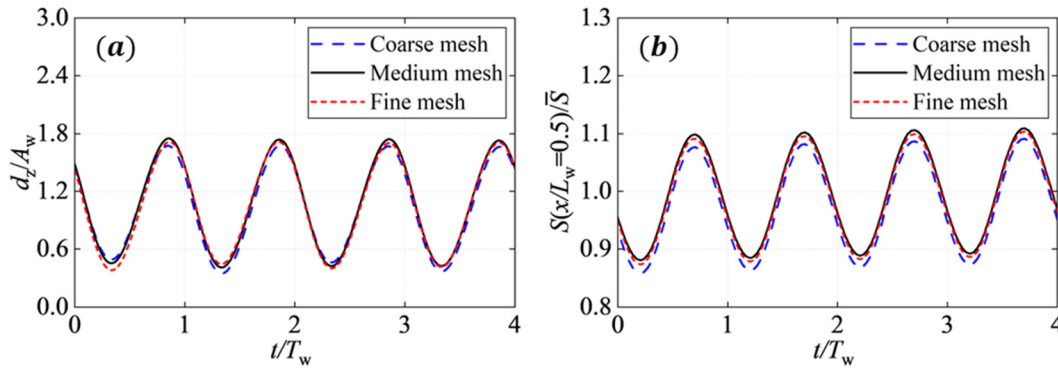


FIG. 6. Time history curves of FSI simulation results in the grid convergence test: (a) Heave displacement (d_z) of the S3 tube's bow. (b) Cross-sectional area at the S3 tube's midsection (\bar{S} denotes the time-averaged value of the cross-sectional area).

Components (a) and (b) originate from the bulge wave and its reflection, while component (c) results from external wave penetration through the flexible tube wall. For a given S3 device, the wavelengths and periods of components (a) and (b) remain constant. However, variations in external wave conditions alter the internal superimposed wave, influencing its wavelength. According to the linear model proposed by Babarit *et al.*,¹⁷ the waveforms of standing waves within the S3 tube can be approximated using sine and cosine functions with a spatial period of $2L_t/n$, leading to the standing wave condition

$$\lambda_t = \frac{2L_t}{n}, \tag{8}$$

where λ_t is the wavelength of the internal superimposed wave.

2. Tube deformation

To capture the standing waves in the S3 WEC, FSI simulations are conducted under various wave periods. Figures 8 and 9 illustrate the deformed tube shape and the amplitude variation of the cross-sectional area $S(x, t)$ for different wave conditions. Despite the relatively small deformation amplitudes, the numerical results successfully capture the 1st, 2nd, and 3rd order standing wave modes, corresponding to Figs. 8(l), 8(e), and 8(a), respectively. However, due to the tube's global motion, pure single mode standing waves are not observed, instead, multiple modes coexist. This phenomenon is consistent with experimental observations.¹

Additionally, the predicted standing wave modes for various wave conditions are summarized in Table IV and compared with Eq. (8). As shown, longer wave periods correspond to longer wavelengths (λ_w) and lower standing wave modes, consistent with the expected relationship in Eq. (8). This indicates that, in the present case, λ_t is primarily influenced by λ_w . To verify this, λ_w is substituted for λ_t in

Eq. (8) to approximate the standing wave mode. The estimated values ($2L_t/\lambda_w$) closely match the predicted standing wave modes (n), as detailed in Table IV. It should be noted that Eq. (8) is an idealized empirical equation and does not account for the effects of the tube's 6DoF motion on standing wave formation.

Furthermore, as indicated by Eq. (8), the tube length (L_t) also affects the formation of standing waves. Specifically, increasing L_t while keeping λ_t constant leads to a transition from lower to higher order standing wave modes. To verify this, a 6 m long tube is examined, with all other geometric parameters and computational settings kept identical to the previously analyzed 3.5 m tube. Figure 10 presents the deformation of the 6 m tube at $T_w = 1.5$ s. The results show that, for the same wave period, increasing the tube length shifts the primary standing wave mode from first mode to second mode, while the deformation amplitude is nearly halved.

E. Fluid field

In the S3 WEC, the interaction between the flexible tube and the surrounding fluids is highly complex due to the combined effects of external water waves and internal pressurized water. The tube undergoes 6DoF motions along with periodic shape deformations, which, in turn, significantly influence both the internal and external flow fields.

Figure 11 illustrates the interaction between the tube and the incident wave at different time instants within one wave period, with wave elevation indicated by color. It is observed that the tube tends to float above the water surface due to its lower density relative to water, disrupting the wave profile and causing nonlinear variations in wave elevation, as highlighted by the white dashed circles in Fig. 11(a). This effect becomes more pronounced for shorter wave periods, as shown in Fig. 11(b), where the incident wave exhibits strong diffraction and intensified surface fluctuations. While such phenomena have been

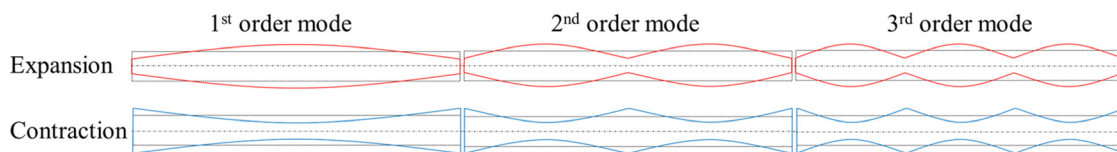


FIG. 7. Schematic diagram of three modes of radial deformation of the S3 WEC: (a) first order mode; (b) second order mode; and (c) third order mode.

12 May 2025 11:42:06

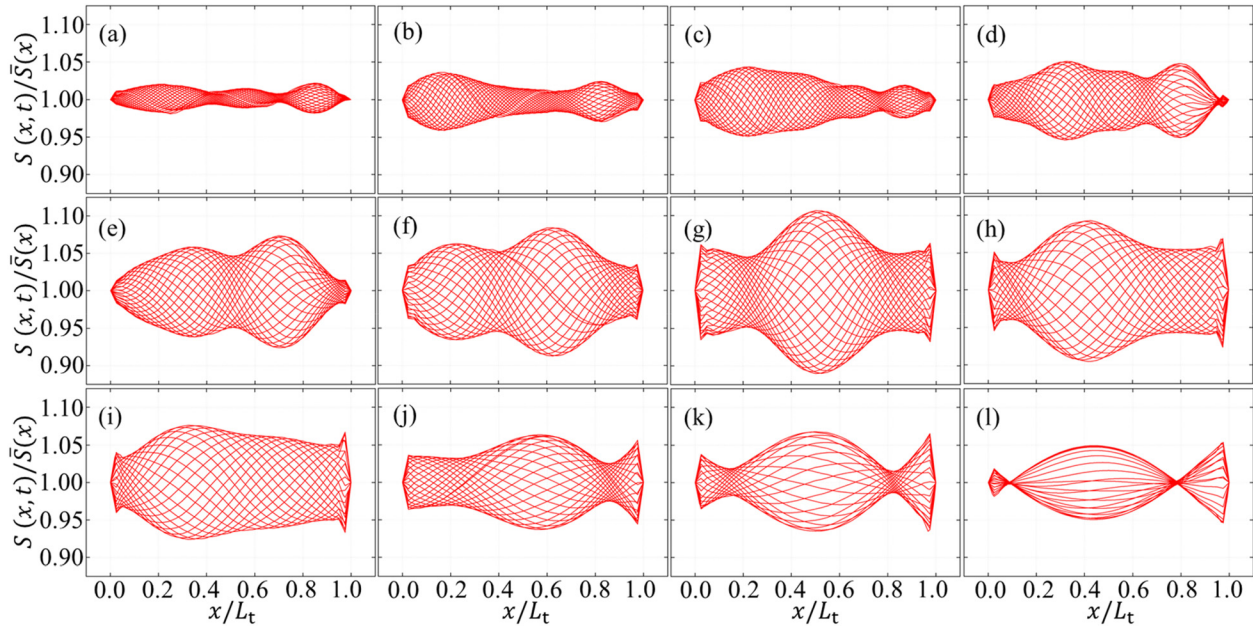


FIG. 8. S3's tube cross-sectional area $S(x, t)$ at different instants within one wave period, normalized by the time-averaged cross-sectional area $\bar{S}(x)$: (a) $T_w = 0.9$ s; (b) $T_w = 1.0$ s; (c) $T_w = 1.1$ s; (d) $T_w = 1.2$ s; (e) $T_w = 1.32$ s; (f) $T_w = 1.4$ s; (g) $T_w = 1.5$ s; (h) $T_w = 1.62$ s; (i) $T_w = 1.7$ s; (j) $T_w = 1.9$ s; (k) $T_w = 2.1$ s; and (l) $T_w = 2.42$ s.

observed in experimental studies,¹ they cannot be accurately captured by previously proposed reduced-order models.^{11,16,17} Additionally, the radiation waves generated by the tube's motion are found to be relatively insignificant.

Regarding the internal flow within the tube, reduced-order models^{11,16,17} typically assume a one-dimensional (1D) flow, where the fluid is considered uniform across each cross section, with variations allowed only along the longitudinal direction. However, our results

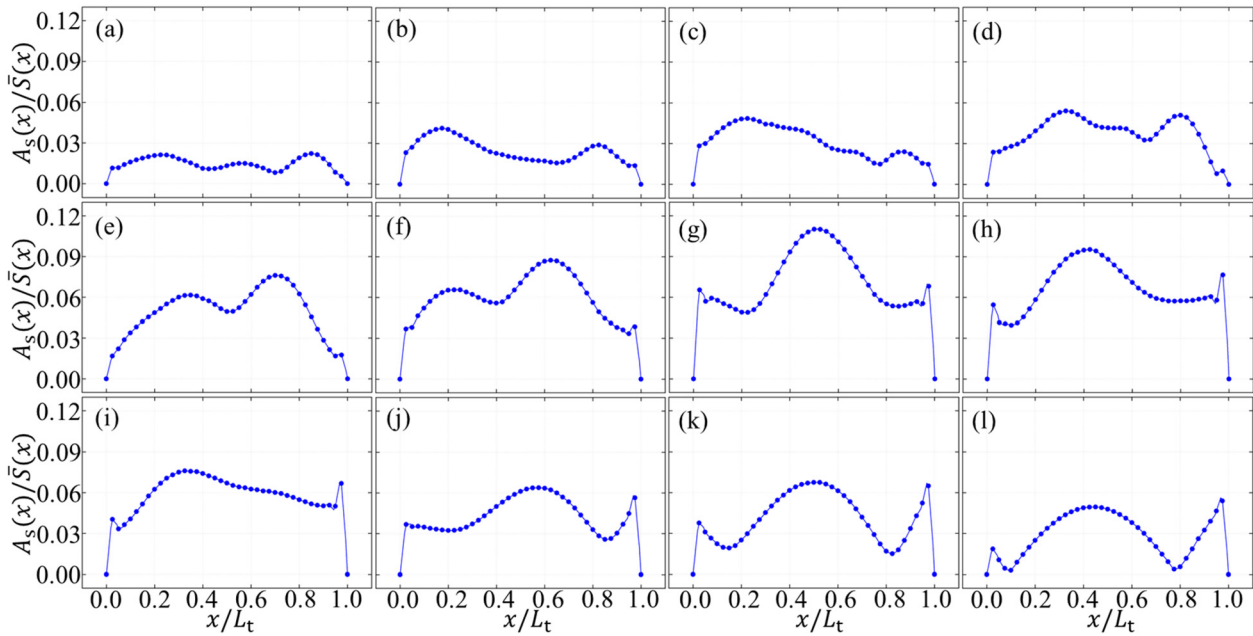


FIG. 9. Variation amplitude of S3's tube cross-sectional area, $A_s(x)$, normalized by the time-averaged cross-sectional area $\bar{S}(x)$: (a) $T_w = 0.9$ s; (b) $T_w = 1.0$ s; (c) $T_w = 1.1$ s; (d) $T_w = 1.2$ s; (e) $T_w = 1.32$ s; (f) $T_w = 1.4$ s; (g) $T_w = 1.5$ s; (h) $T_w = 1.62$ s; (i) $T_w = 1.7$ s; (j) $T_w = 1.9$ s; (k) $T_w = 2.1$ s; and (l) $T_w = 2.42$ s.

TABLE IV. Primary standing wave modes within S3's tube at various wave periods.

Wave period T_w (s)	Wavelength λ_w (m)	Primary standing wave mode n	$2L_t/\lambda_w$
0.90–1.20	1.26–2.25	3 rd order mode	3.11–5.54
1.32–1.62	2.72–4.10	2 nd order mode	1.71–2.57
1.70–2.42	4.51–9.12	1 st order mode	0.77–1.55

reveal a significantly more complex internal flow behavior. As a closed cavity structure, the tube exhibits internal flow variations primarily governed by its local deformations and global motion.

Figures 12 and 13 present the predicted velocity and pressure distributions inside the tube at different time instants within one wave period, revealing a highly three-dimensional flow field. The internal fluid motion can be primarily decomposed into two components: a reciprocating motion along the tube's longitudinal axis and a local rotational motion at each cross section. The former results from the periodic expansion and contraction of the tube's radial area, while the latter is mainly induced by the tube's global heave and sway motions. Notably, the rotational motion of the internal fluid is observed here for the first time, to the best of our knowledge. This phenomenon has not been reported in existing experimental studies, likely due to limitations in internal flow field measurement techniques. Moreover, reduced-order models^{11,16,17} typically adopt one-dimensional flow assumptions, which are inherently incapable of capturing such rotational behavior.

To further investigate the reciprocating motion, we focus on a specific location along the tube at $x/L_t = 0.5$, highlighted by a red circle in Fig. 12(a). During $0 \leq t \leq 0.5T_w$, as indicated by the red arrows, fluid flows toward this region, causing local tube expansion, which is reflected in the time history of $S(x, t)$ in Fig. 14(b). This expansion leads to an increase in pressure, as shown in Fig. 13(b). Conversely, during $0.5T_w \leq t \leq 1.0T_w$, fluid flows outward from $x/L_t = 0.5$ toward both ends of the tube, resulting in contraction and a corresponding decrease in $S(x, t)$ and pressure. This behavior aligns with the observations of Farley *et al.*¹²

The rotational motion is analyzed in Fig. 12(b), where the cross section at $x/L_t = 0.5$ is selected, as it exhibits the most significant shape deformation. The fluid consistently rotates counterclockwise (red arrows) relative to its center (red triangles). Due to the tube's global heave motion, when the tube moves upward, the fluid rotation center

shifts in the positive y -direction, and vice versa. This rotational flow is attributed to the asymmetric forces exerted by the tube wall on the internal fluid, caused by the coupling of heave and sway motions. The direction of rotation appears to be governed by the phase and direction of the tube's global movement; however, the precise mechanism and its quantitative relationship require further investigation.

A distinct feature of the S3 WEC is its closed-end design. The simulation results clearly demonstrate that fluid movement toward the tube's ends generates dynamic interactions with the structure, causing abrupt changes in fluid velocity and direction. These interactions increase fluid loading on the bow and stern, potentially raising concerns regarding structural failure, as indicated by the tube deformation in Fig. 9(l).

F. Structural responses

The structural response of the S3 WEC is analyzed under the wave condition that induces the maximum radial deformation, specifically at $T_w = 1.5$ s. Figure 15 presents the strain and stress distributions along the tube surface at four different time instants within one wave period. The results indicate that stress and strain levels are relatively low at both ends of the tube due to minimal deformations, whereas the central section, experiencing larger deformations, exhibits significantly higher stress and strain.

In conjunction with the time history of $S(x, t)$ shown in Fig. 14, the propagation of the bulge wave is clearly observed in Fig. 15(a), with its peak highlighted by a black circle. As the bulge wave propagates, $S(x, t)$ increases at its peak location, leading to a corresponding rise in stress and strain levels at that point.

G. Power output

To evaluate the power output performance of the S3 WEC, the PTO module is introduced in this section. In the S3 WEC, DEG PTO

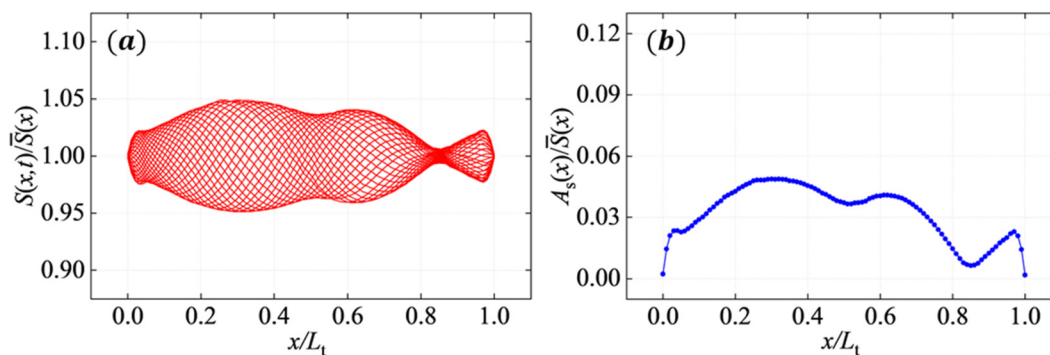


FIG. 10. Deformation of the S3 WEC with a 6 m long tube: (a) tube cross-sectional area $S(x, t)$ at different instants within one wave period ($T_w = 1.5$ s), normalized by the time-averaged cross-sectional area $\bar{S}(x)$. (b) Variation amplitude of tube cross-sectional area, $A_s(x)$, normalized by the time-averaged cross-sectional area $\bar{S}(x)$.

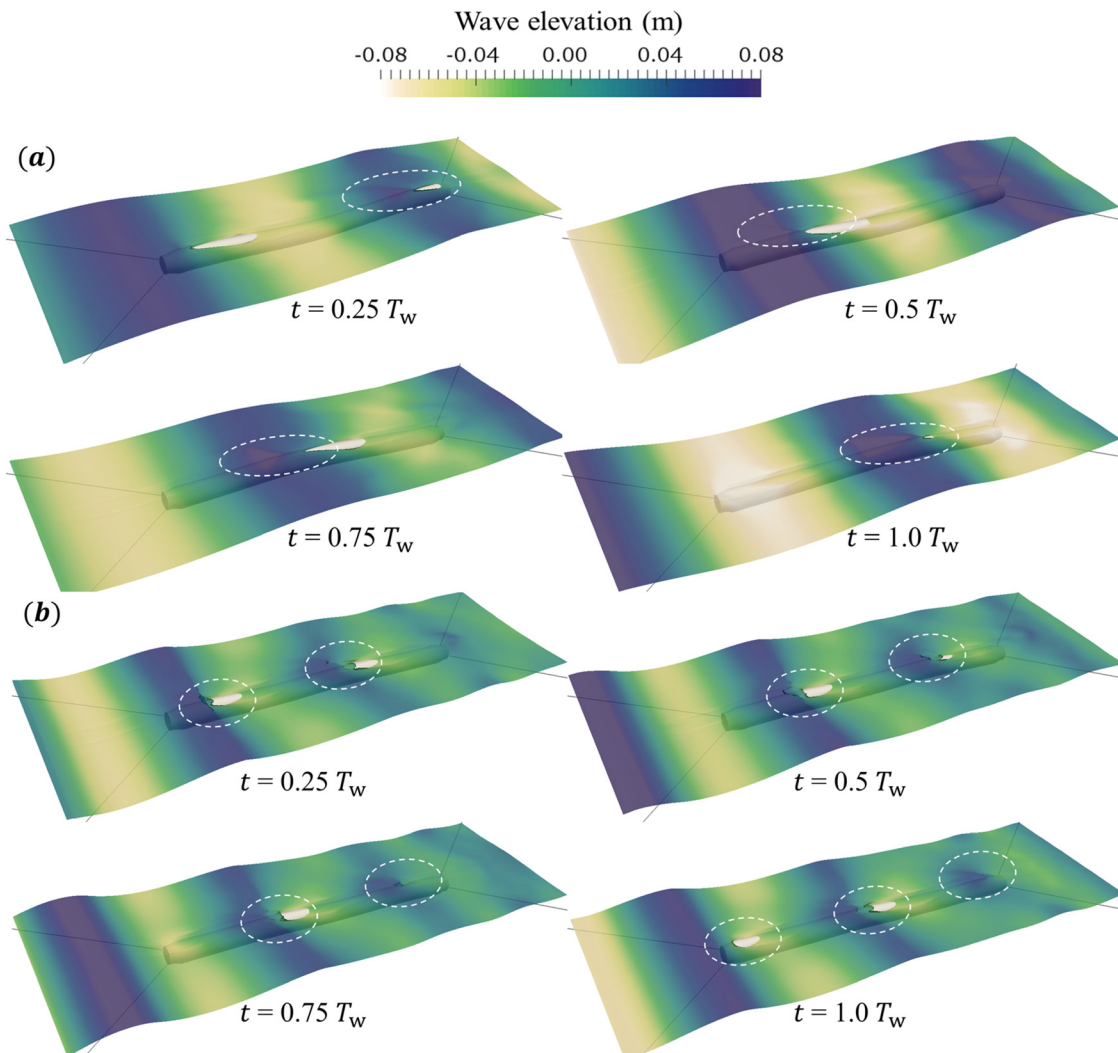


FIG. 11. Interactions between the S3's tube and incident waves at different instants within one wave period: (a) $T_w = 1.5$ s and (b) $T_w = 1.0$ s.

units are utilized to harvest energy from tube deformation. As illustrated in Fig. 16(a), each DEG PTO can be modeled as a variable capacitor, with capacitance varying in response to the tube's expansion and contraction. When integrated with an external conditioning circuit, this system enables electrical energy generation. In this study, the conditioning circuit proposed by Moretti *et al.*⁴² is adopted to estimate the power output of the S3 WEC, with relevant parameters summarized in Table V.

It should be noted that the PTO module is not considered in the present simulations. This omission does not affect the qualitative discussions and physical insights presented above, while it influences certain quantitative results, such as the resonant frequency and deformation amplitude. A more comprehensive evaluation of the PTO's impact on the dynamic response of the S3 WEC will be explored in a forthcoming study.

Figure 16(b) depicts a typical energy conversion cycle, which can be divided into four phases: (1) expansion, (2) priming, (3) harvesting, and (4) discharging. The electrical energy output, W_e , is represented by the shaded area enclosed by three lines in the figure. Further details on the DEG PTO energy conversion process and the associated control circuit can be found in Moretti *et al.*⁴² The electrical energy generated by the i th DEG PTO per cycle is given by

$$W_{e,i} = \frac{1}{2} C_B V_B^2 - \frac{1}{2} C_A V_A^2 + \frac{1}{2} C_a (V_B^2 - V_A^2), \quad (9)$$

where C_A and C_B are the capacitances of the DEG at different phases, V_A and V_B are the corresponding voltages, and C_a is a constant capacitor charged to a fixed voltage V_0 . The total electrical energy (W_t) generated by the S3 WEC per wave period and the corresponding time-averaged power output (P_t) are calculated as

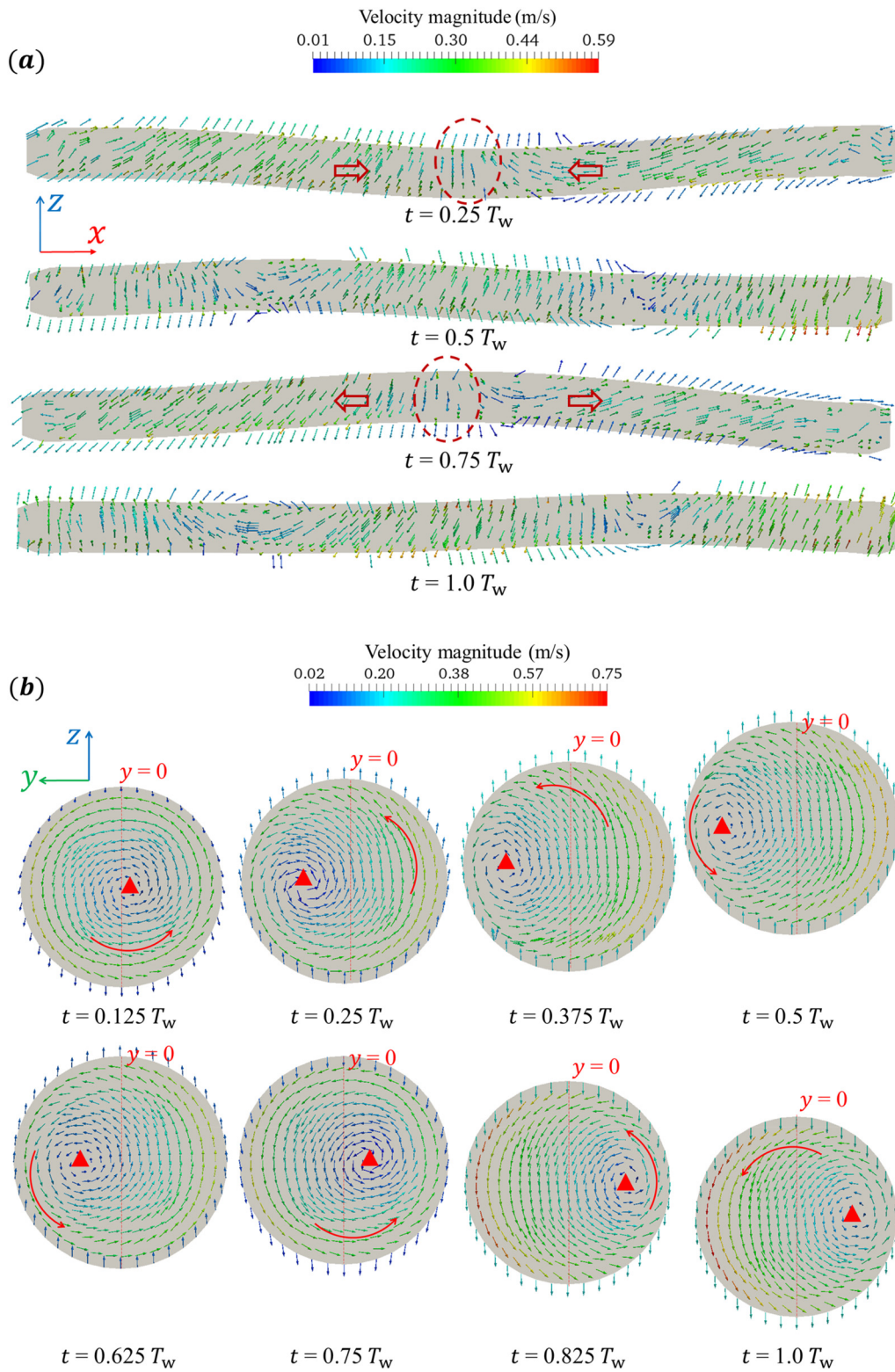


FIG. 12. Fluid velocity distribution at different sections of the S3's tube at different instants within one wave period ($T_w = 1.5$ s): (a) $y = 0$ and (b) $x/L_t = 0.5$.

12 May 2025 11:42:06

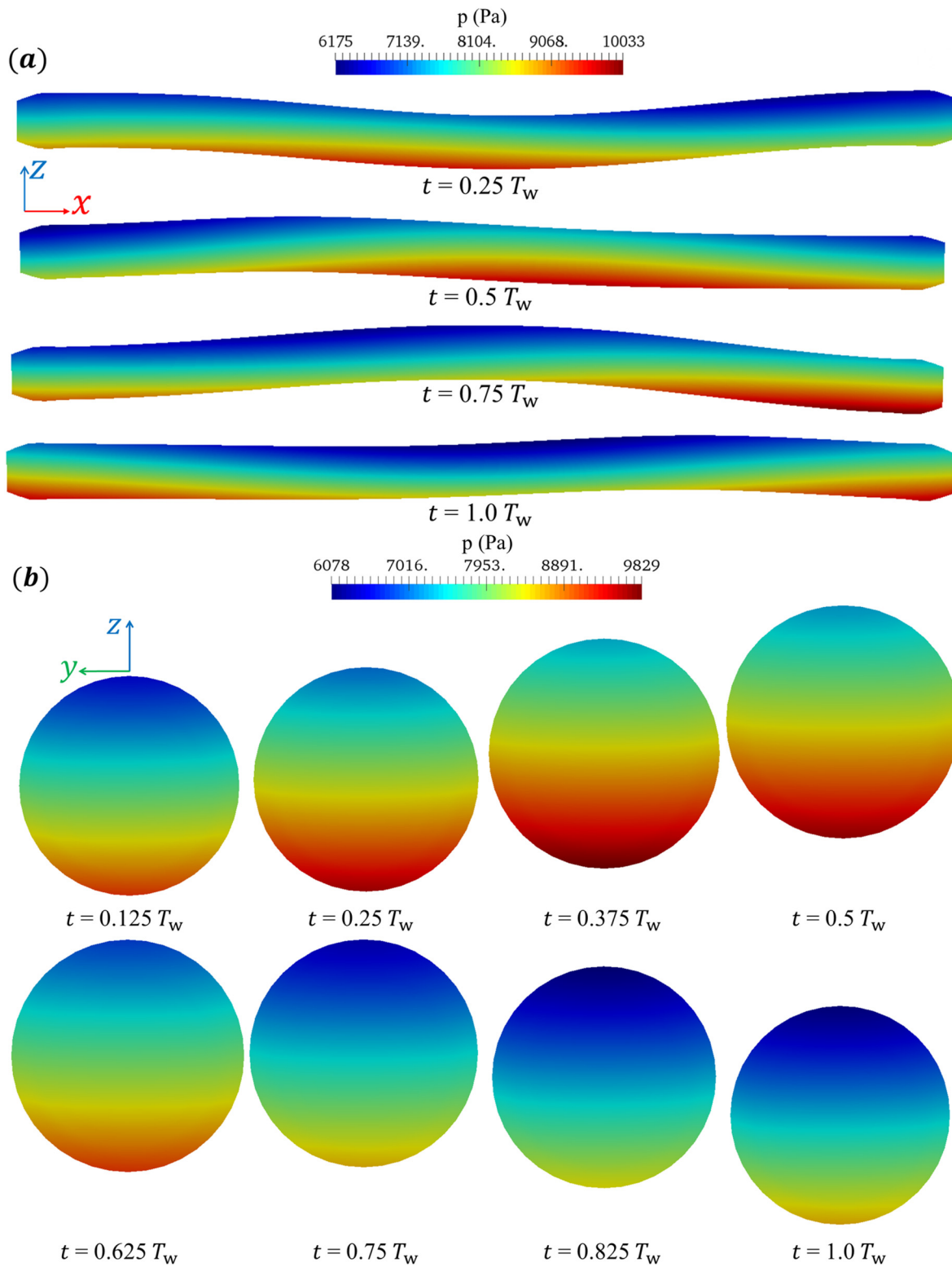


FIG. 13. Pressure distribution at different sections of the S3's tube at different instants within one wave period ($T_w = 1.5$ s): (a) $y = 0$ and (b) $x/L_1 = 0.5$.

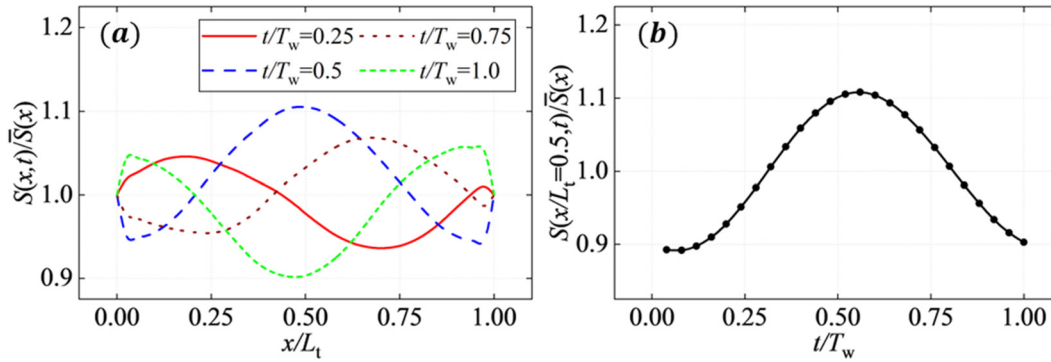


FIG. 14. S3's tube deformation at different instants within one wave period ($T_w = 1.5$ s): (a) $0 \leq x/L_t \leq 1$ and (b) $x/L_t = 0.5$.

$$W_t = \sum_i^N W_{e,i}, P_t = W_t/T_w, \quad (10)$$

where N denotes the number of DEG PTO units.

Figure 17 illustrates the variation of W_t and P_t with the incident wave period (T_w). Both parameters initially increase with T_w , reaching a peak at $T_w = 1.5$ s before gradually decreasing. The power output remains relatively high within the range of $T_w = 1-2$ s, which corresponds to typical ocean wave conditions based on a scaling factor of 30.

For a full-scale device with a tube length of 105 m, P_t is estimated to range from ~ 131 to 310 kW. This estimation is based on the Froude similarity principle, following approaches adopted in previous experimental and numerical studies.^{11,17} The viscous effects and flexible material properties may introduce some scale-dependent discrepancies, which is a focus of our next-step study.

It should be noted that these estimations are based on relatively small tube deformations, without optimization of tube dimensions or conditioning circuit parameters. Additionally, energy losses throughout the conversion process have not been accounted for, which may affect the actual power output.

IV. ANACONDA WEC MODELING

A. Physical model

The Anaconda model analyzed in this study is based on the experimental setup of Mendes *et al.*,¹³ as illustrated in Fig. 18. The motion of the tube's bow is constrained by a mooring line, while the stern is fixed. Notably, the laboratory experimental Anaconda model differs from the actual device, primarily in the design of the PTO system at the tube's stern. In the real device, the PTO typically consists of a fluid-driven pump or turbine, and the tube's stern is fully enclosed. However, for lab testing convenience, a fixed vertical tube with an orifice plate was used in place of the actual PTO, resulting in an open-end configuration that is exposed to air. To maintain the necessary pre-stretching of the flexible horizontal tube, the water level inside the vertical tube was kept higher than the external water level.

Unlike the experiments,^{11,13} which introduced PTO via an orifice plate, the numerical simulations employ a porous media model to represent PTO. This approach simplifies CFD-FEA mesh generation while improving numerical stability. According to Eq. (2), the porous media is modeled as a body force term f_p , defined by the Darcy-Horkheimer equation⁴³

$$f_p = -\left(\mu D_c + \frac{1}{2}\rho|U|F_c\right)U, \quad (11)$$

where D_c and F_c are coefficients representing viscous and inertial losses, respectively. The term D_c is proportional to velocity, indicating viscous losses, while F_c is proportional to the square of velocity, representing inertial losses. These coefficients are determined by the physical properties of the porous medium. In this study, a homogeneous porous medium with linear damping is selected, setting $F_c = 0$. The viscous damping coefficient is set to $D_c = 2 \times 10^{10}$ to ensure high impedance.

Additionally, in the numerical simulations, the mooring line is modeled as a horizontal spring with a length of 1 m and a stiffness of 1×10^3 N/m. Key parameters of the model are illustrated in Fig. 18, while the material and mooring line properties are summarized in Table VI.

B. Computational setup

A hexahedral computational domain is employed in this study, as illustrated in Fig. 19. The Anaconda model is centrally positioned within the domain, maintaining a 1.2 m distance from both the inlet and outlet boundaries. The water depth is set to 1.9 m. To monitor the flow field, observation points are strategically placed along the tube and inside the air chamber.

To accurately capture the FSI responses, a structured mesh is used to define the interface between the fluid and solid domains. The minimum grid size on the flexible tube's surface is set at 0.04 m (x) \times 0.012 m (y) \times 0.012 m (z). Additionally, local grid refinement is applied around the tube and near the free surface to enhance the resolution of hydrodynamic forces and accurately capture the tube's 6DoF motion.

The boundary conditions are defined as follows: the inlet velocity is prescribed based on the incident wave parameters, while a zero-gradient condition is imposed at the outlet, front, and back boundaries. A pressure outlet condition is applied at the top boundary, and a no-slip condition is enforced at the bottom boundary.

To examine the resonant responses of the Anaconda WEC, simulations are conducted under various regular wave conditions, as summarized in Table VII.

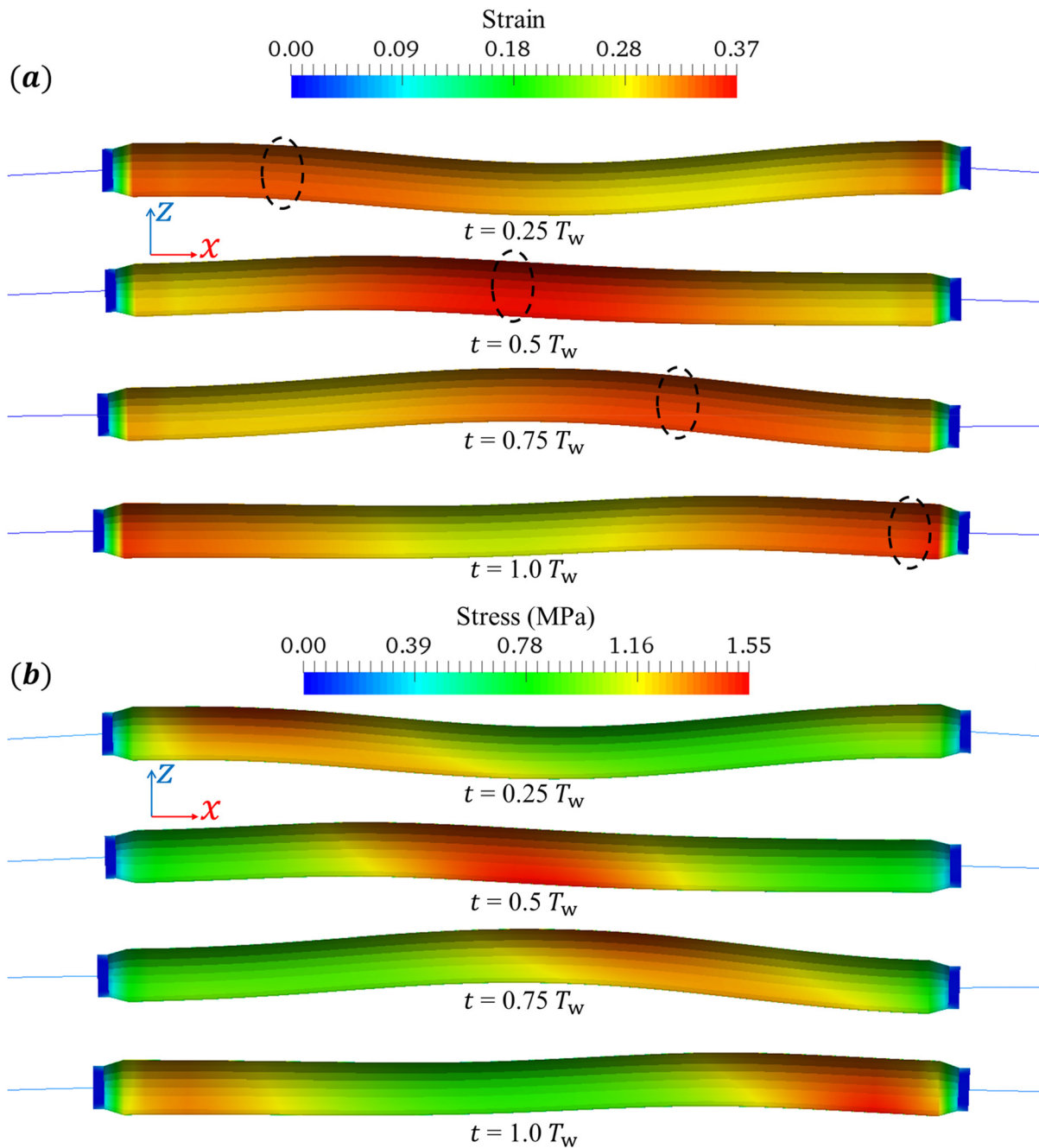


FIG. 15. Structural responses of the S3 WEC at different instants within one wave period ($T_w = 1.5$ s): (a) strain distribution and (b) stress distribution.

C. Grid convergence test

A grid independence test is performed to determine an optimal mesh resolution that ensures a balance between computational accuracy and efficiency. Three sets of meshes with varying resolutions are generated, with the minimum grid sizes on the tube surface and total grid numbers summarized in Table VIII. A regular wave with a

frequency of 0.65 Hz (f_w) and an amplitude of 0.05 m (A_w) is selected for the test. The time step is set to $2 \times 10^{-3} T_w$, where $T_w = 1/f_w$, ensuring that the CFL condition is satisfied ($CFL < 1$).

Figure 20 compares the predicted water elevation in the vertical tube and the heave displacement at the tube's midpoint for different mesh resolutions. The results from the medium and fine meshes show

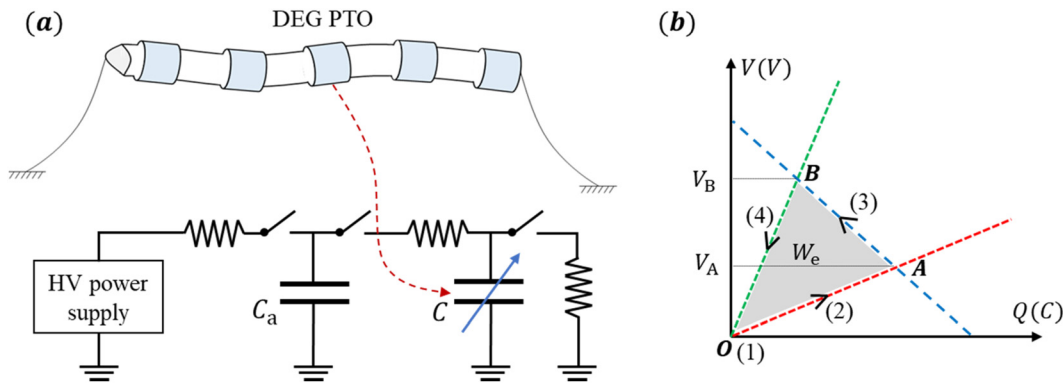


FIG. 16. (a) Conditioning circuit for the DEG PTO. (b) Charge-voltage plane and example of conversion cycle.

TABLE V. Conditioning circuit parameters.

Name	Symbol	Value	Unit
Dielectric constant of tube	ϵ_r	5.25	...
Permittivity of free space	ϵ_0	8.85×10^{-12}	F/m
Constant capacitor	C_A	3.0×10^{-7}	F
Voltage applied to constant capacitor	V_0	1.5×10^4	V

close agreement, indicating that further refinement does not significantly improve accuracy. Therefore, the medium mesh with a time step of $2 \times 10^{-3} T_w$ is selected for the subsequent simulations.

D. Resonant responses

1. Resonant conditions

Unlike the S3 WEC, where resonance occurs due to the formation of standing waves within the tube, resonance in the Anaconda WEC requires not only the presence of standing waves but also that the tube's stern aligns with an anti-node to maximize power output at the PTO. Furthermore, the boundary conditions at the tube's stern

differ between the two devices: in the S3 WEC, a rigid wall at the stern results in complete reflection of the internal fluid, whereas in the Anaconda WEC, the boundary condition depends on the impedance of the PTO. These differences create distinct resonance conditions for each system.

Experimental studies by Chaplin *et al.*¹¹ and Farley *et al.*¹⁶ suggest that resonance in the Anaconda WEC occurs when the external water wave speed matches the internal bulge wave speed of the flexible tube. As the bulge wave speed remains constant, the corresponding resonance frequency is denoted as f_{R1} . Additionally, in the present Anaconda model, the presence of an OWC within the vertical tube and the heave motion of the tube's bow introduce two additional resonance frequencies: one corresponding to the natural frequency of the OWC (f_{R2}) and the other to the natural frequency of the tube's heave motion (f_{R3}).

To determine the bulge wave speed in the horizontal flexible tube (T1) and the natural frequency of the OWC in the vertical rigid tube (T2), a free-decay test is conducted, as illustrated in Fig. 19. Initially, a water column with a height of 0.6 m in T2 flows into T1, which has an initial radius of 0.07715 m. This induces periodic contraction and expansion in T1 until the water level in T2 stabilizes at 0.2271 m. After reaching a quasi-steady state, the radius of T1 is increased to 0.08268 m. The variations in water surface elevation, pressure, and

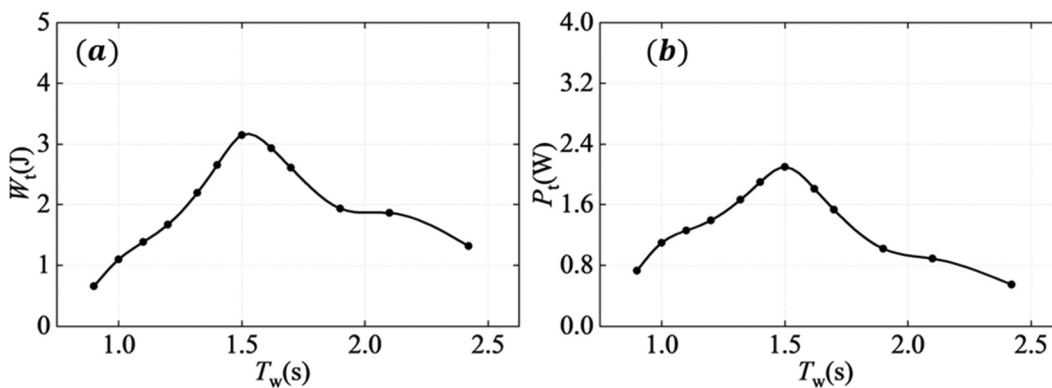


FIG. 17. Power performance of the S3 WEC at different wave periods: (a) electrical energy within one wave period and (b) time-averaged power output.

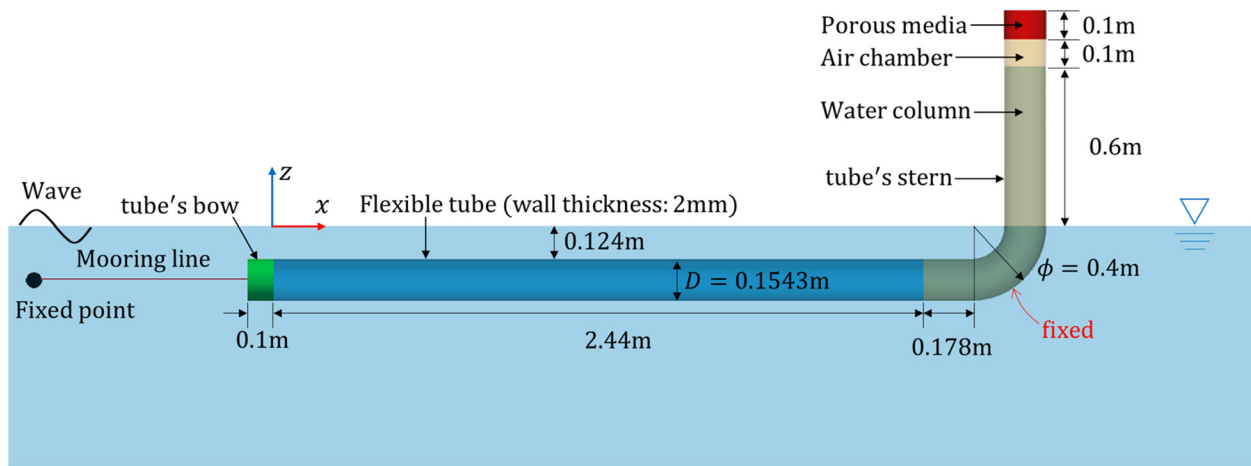


FIG. 18. Schematic diagram of the Anaconda model.

tube cross-sectional area at different locations (M1–M5) are shown in Fig. 21. Using the data in Fig. 21(a), the OWC oscillation period is determined to be 19.2s, corresponding to a natural frequency of $f_{R2} = 0.052$ Hz.

TABLE VI. Material properties of the Anaconda model.

Component	Material	Density (kg/m ³)	Young's modulus (MPa)	Poisson's ratio
Flexible tube	Rubber	960	0.91	0.49
Tube's bow	Wood	700	8100	0.35
Tube's stern	Acrylic	1190	3030	0.37

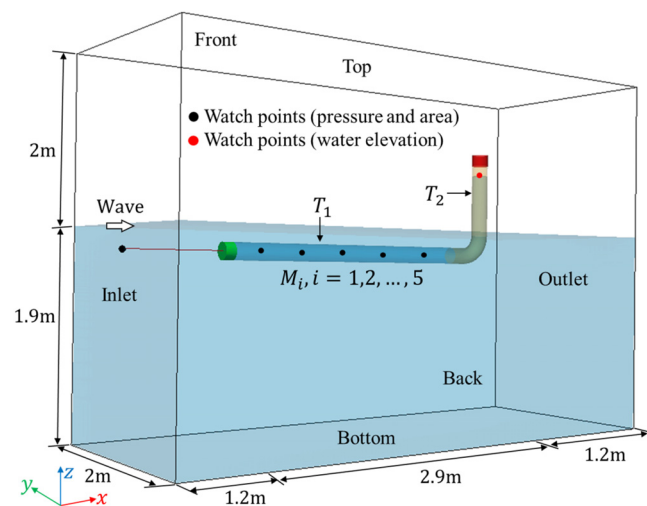


FIG. 19. Computational domain for the Anaconda WEC modeling.

According to the linear theory proposed by Lighthill,⁴⁴ the bulge wave speed (C_b) in a homogeneous tube is related to the distensibility (D_t) and water density (ρ_w) as follows:

$$C_b = \frac{1}{\sqrt{\rho_w D_t}} \quad \text{and} \quad D_t = \frac{1}{S} \frac{\partial S}{\partial p}, \quad (12)$$

where S represents the tube's cross-sectional area and p denotes the pressure difference across the tube wall. Using Eq. (12) and data from Fig. 21(b), the calculated bulge wave speed is 3.78 m/s, assuming a water density of 1025 kg/m³. Resonance is expected when the external water wave speed (C_w) matches this value. Based on Stokes wave theory,⁴⁵ at a water depth of 1.9 m, the wave frequency corresponding to a phase velocity of 3.78 m/s is determined to be 0.31 Hz; thus, $f_{R1} = 0.31$ Hz.

To determine the natural frequency of the tube's heave motion, a second free-decay test is conducted after the tube reaches a quasi-steady state. In this test, the tube's bow is displaced 0.15 m below its equilibrium position and then released to oscillate freely. The time history of the bow's heave displacement is shown in Fig. 22(a), and a fast Fourier transform (FFT) is applied to identify the dominant frequency. As illustrated in Fig. 22(b), the primary peak occurs at 0.65 Hz, indicating that $f_{R3} = 0.65$ Hz.

2. Tube deformation

Further analysis is conducted on the bulge wave formation at the resonant frequencies of 0.31 Hz (f_{R1}) and 0.65 Hz (f_{R3}). Figure 23 illustrates the variation of $S(x, t)$ over time and space, where the black dashed line marks the position of the maximum $S(x)$ at different

TABLE VII. Wave conditions for the Anaconda WEC modeling.

Wave frequency f_w (Hz)	Wave speed C_w (m/s)	Wave amplitude A_w (m)	Wavelength λ_w (m)
0.1–1.0	1.56–4.28	0.05	1.56–42.83

TABLE VIII. Mesh Information for the grid independence study of the Anaconda WEC model.

Mesh type	Grid size (m)	Total grid number ($\times 10^6$)
Coarse mesh	0.06 (x) \times 0.015 (y) \times 0.015 (z)	0.78
Medium mesh	0.04 (x) \times 0.012 (y) \times 0.012 (z)	1.06
Fine mesh	0.03 (x) \times 0.008 (y) \times 0.008 (z)	1.56

instants, representing the peak of the bulge wave. Within one wave period, the bulge wave propagates from the bow to the stern (red arrow) and then reflects toward the bow (blue arrow). Under resonant conditions, the peak of the bulge wave consistently reaches its maximum at the stern, aligning with the observations of Chaplin *et al.*¹¹ Additionally, as shown in Fig. 24, the deformation amplitude at f_{R3} is significantly greater than at f_{R1} .

At both f_{R1} and f_{R3} , the tube’s deformation amplitude follows a pattern of being larger at the ends and smaller in the middle, with the stern experiencing greater deformation than the bow. This trend is further supported by the pressure distribution along the tube’s central axis, as shown in Fig. 25. The internal pressure exhibits a characteristic

decrease followed by an increase from the bow to the stern, which is particularly pronounced at f_{R3} .

E. Flow field

To better understand the internal and external flow characteristics of the Anaconda WEC, the scenario with the greatest tube deformation ($f_w = 0.65$ Hz) is selected for analysis. Figure 26 illustrates the interaction between the Anaconda and the incident waves. Similar to the S3, the Anaconda’s tube, having a lower density than water, tends to float above the water surface, causing nonlinear variations in wave elevation, as indicated by the white circles.

As shown in Fig. 27, the internal flow dynamics of the Anaconda resemble those observed in the S3, with the internal fluid undergoing reciprocating motion along the tube due to periodic radial expansion and contraction. However, unlike the S3, the Anaconda’s internal fluid does not exhibit rotational motion. This difference arises primarily from the distinct boundary conditions at the stern of the two devices, as discussed earlier. In particular, the motion of the OWC in the Anaconda, especially within T2 at the stern, significantly influences the fluid flow direction inside the tube.

Additionally, the pressure distribution within the Anaconda’s tube, shown in Fig. 28, closely follows the variation of $S(x, t)$ in Fig. 29,

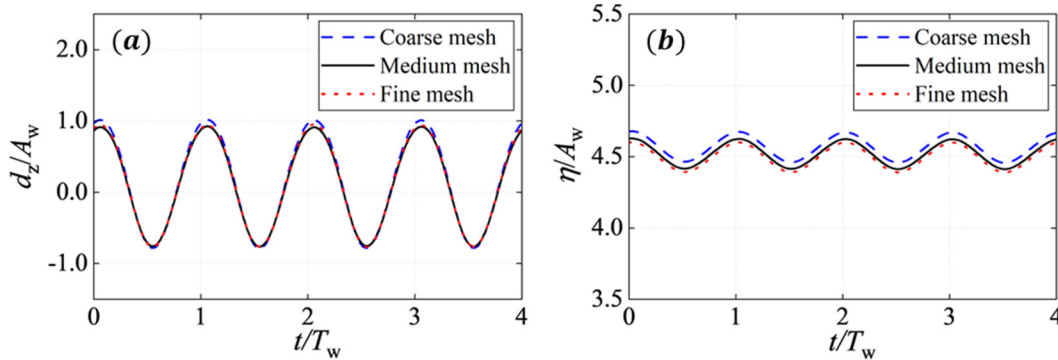


FIG. 20. Time history curves of FSI responses in the grid independence study: (a) heave displacement at the tube’s midpoint and (b) water surface elevation in the vertical tube.

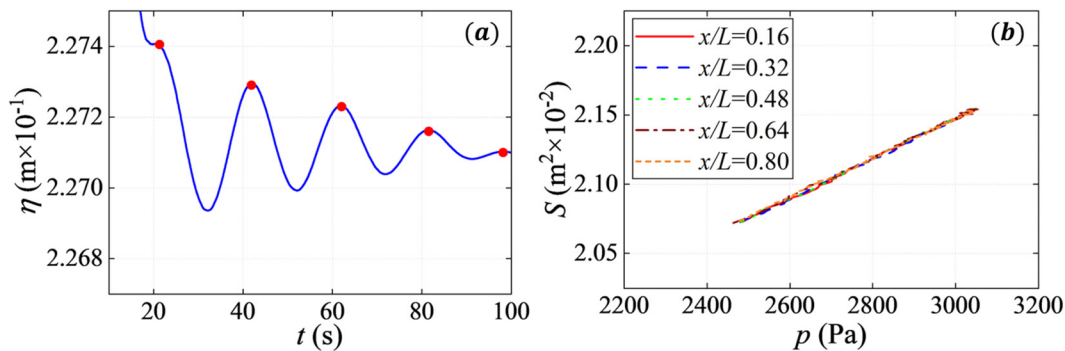


FIG. 21. (a) Time history of water elevation in T2 (red points represent the local maximum). (b) Anaconda’s tube cross-sectional area varies with pressure at different positions in T1.

12 May 2025 11:42:06

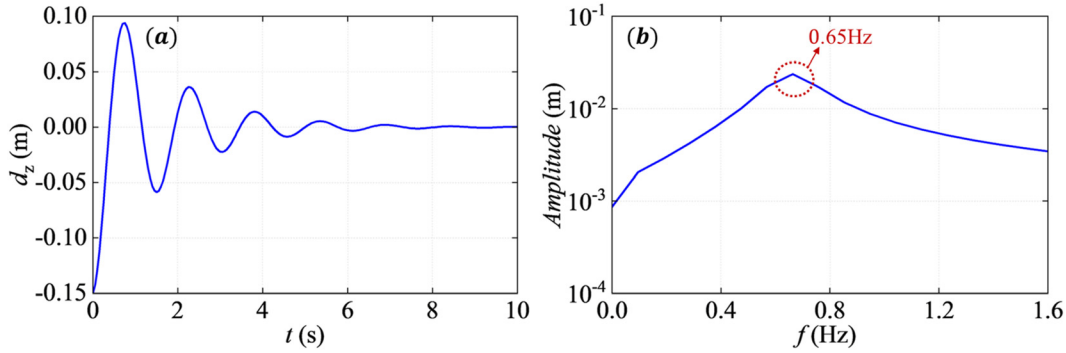


FIG. 22. (a) Time history of the vertical displacement of the Anaconda tube's bow during the second free decay test. (b) Results after applying FFT to the time history data.

mirroring the relationship observed in the S3. In this case, pressure is positively correlated with $S(x, t)$.

F. Structural responses

Figure 30 presents the strain and stress distribution when the tube deformation amplitude reaches its maximum ($f_w = 0.65$). The propagation of the bulge wave along the tube is clearly observed, with regions of high strain in Fig. 30(a) corresponding to the wave's peak. During $0T_w \leq t \leq 0.5T_w$, the bulge wave travels from left to right, while in $0.5T_w \leq t \leq 1.0T_w$, it propagates in the opposite direction.

The maximum stress is primarily concentrated at the tube's stern. This is partly due to the larger deformation amplitude in this region and partly because, while the tube's bow can move, the stern remains fixed. As a result, the bow is positioned higher than the stern, placing the stern in a stretched state and leading to increased stress. It is important to note that under real operating conditions, both ends of the Anaconda WEC are not fixed but instead connected to the seabed via mooring lines, similar to the S3 WEC.

G. Power output

In this study, a porous media model is employed to simulate the PTO of the Anaconda WEC. Consequently, the power output of WEC system is estimated using the following equations:

$$\bar{P} = \frac{1}{T_w} \int_0^{T_w} p(t)Q(t)dt, \quad (13)$$

$$CW = (\bar{P}T_w) / \left(\frac{1}{2} \rho_w g A_w^2 C_w \right), \quad (14)$$

where \bar{P} represents the cycle-averaged power generated by the WEC, CW is the capture width, p denotes the space-averaged pressure in the air chamber below the porous media, and Q is the volume flux across the porous media.

Figure 31 illustrates the power performance of the Anaconda WEC across different wave frequencies. A peak in both \bar{P} and CW/D is observed at $f_w = 0.65$ Hz (f_{R3}), driven by the resonance of the tube's heave motion. A smaller peak appears at $f_w = 0.31$ Hz (f_{R1}), resulting from the resonant response induced by the bulge wave. Comparing the power outputs at f_{R1} and f_{R3} , it is evident that resonance driven by tube heave motion generates significantly higher power amplitudes than that induced by the bulge wave.

To compare the power output of different flexible tube WECs, the performance of an Anaconda WEC with the same tube length (105 m) as the S3 WEC is estimated using Froude scaling law. Based on Fig. 31(a), the maximum power output of device is ~ 78 kW, significantly lower than the 310 kW of the S3 WEC. This highlights the advantages of the distributed PTO system employed in the S3 WEC.

V. DISCUSSIONS

High-fidelity FSI simulations of flexible tube WECs are particularly challenging. Difficulties arise not only from the slender, thin-walled nature of the tube but also from the requirement for robust

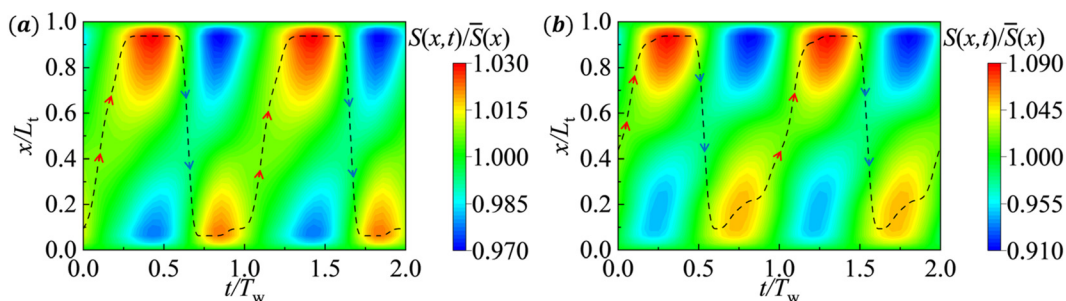


FIG. 23. Time and spatial variation of the cross-sectional area $S(x, t)$ of the Anaconda's tube, normalized by the time-averaged cross-sectional area $\bar{S}(x)$: (a) $f_w = 0.31$ Hz and (b) $f_w = 0.65$ Hz.

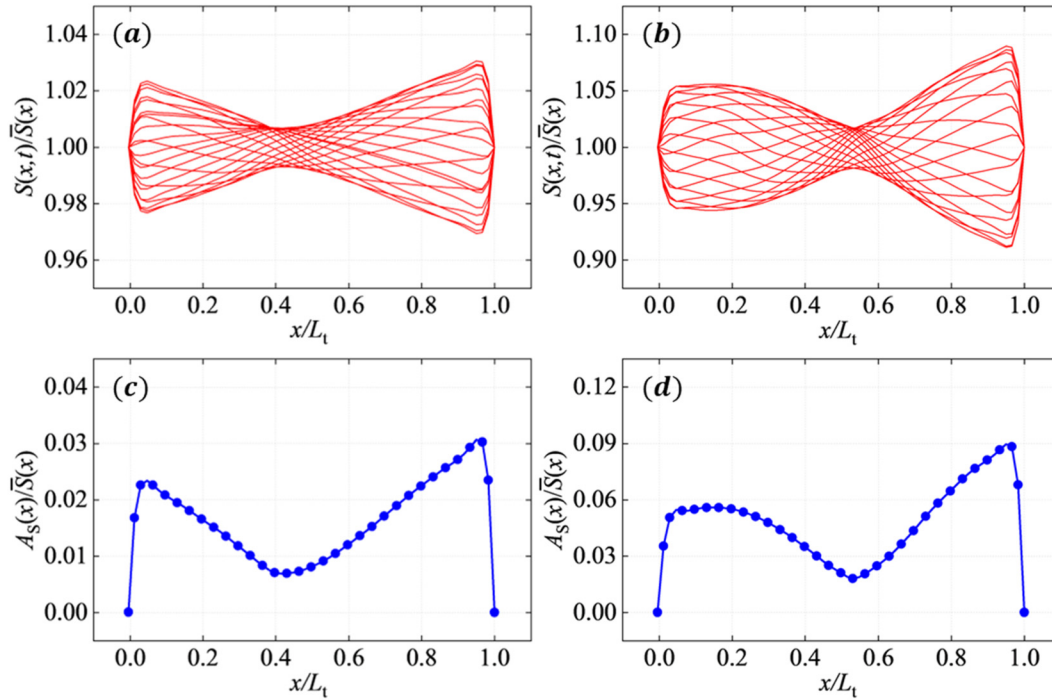


FIG. 24. Instantaneous cross-sectional area $S(x, t)$ and its variation amplitude $A_S(x)$ of the Anaconda's tube, normalized by the time-averaged cross-sectional area $\bar{S}(x)$: (a) $f_w = 0.31$ Hz, $S(x, t)$; (b) $f_w = 0.65$ Hz, $S(x, t)$; (c) $f_w = 0.31$ Hz, $A_S(x)$; and (d) $f_w = 0.65$ Hz, $A_S(x)$.

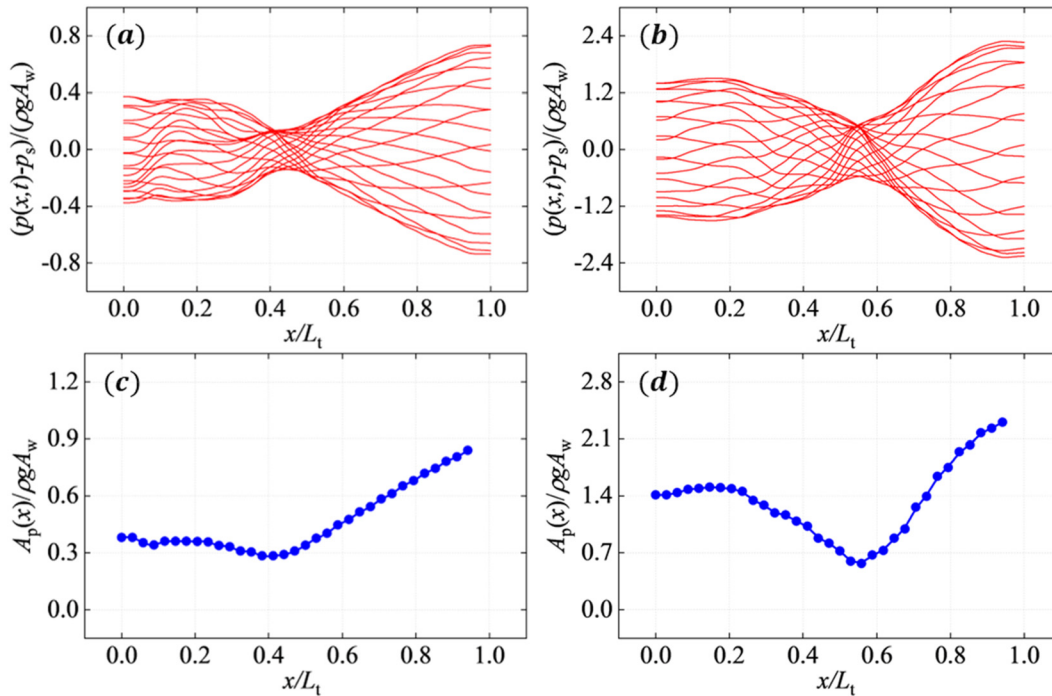


FIG. 25. Instantaneous pressure $p(x, t) - p_s$ ($p_s = 2023$ Pa is the hydrostatic pressure) and its variation amplitude $A_p(x)$ at the centerline of the Anaconda's tube, normalized by $\rho g A_w$: (a) $f_w = 0.31$ Hz, $p(x, t) - p_s$; (b) $f_w = 0.65$ Hz, $p(x, t) - p_s$; (c) $f_w = 0.31$ Hz, $A_p(x)$; and (d) $f_w = 0.65$ Hz, $A_p(x)$.

12 May 2025 11:42:06

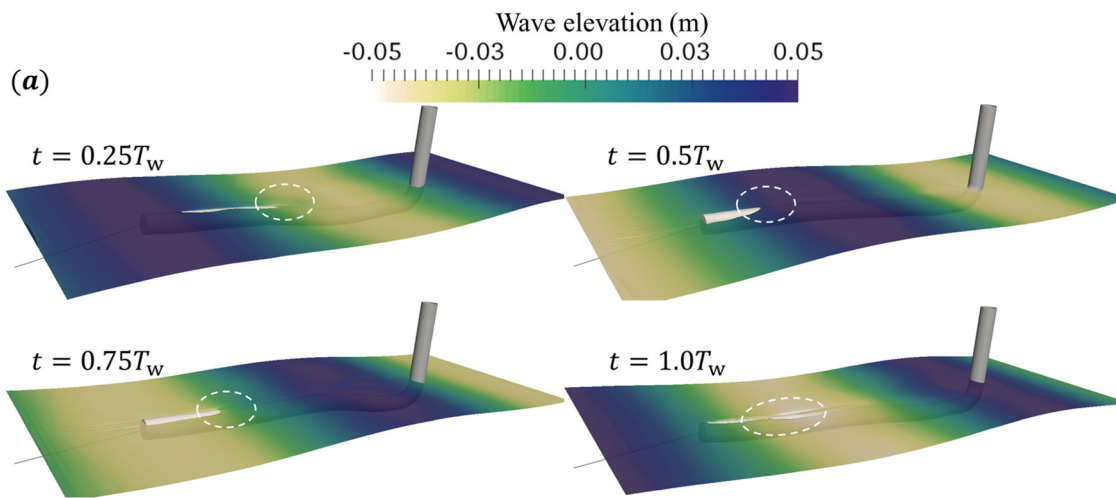


FIG. 26. Interactions between the Anaconda WEC and incident waves at a wave frequency of 0.65 Hz.

bidirectional coupling among the internal fluid, external fluid, and structural domains. Moreover, simulating the internal flow field driven by the deformation of a fully two-ends enclosed flexible tube further increases the complexity. Such simulations impose stringent demands on the geometric model, mesh quality from both fluid field and structural field, time step, numerical discretization schemes, and coupling strategy, as any deficiencies can lead to numerical solution divergence. Consequently, to ensure simulation stability, the geometry dimensions of the flexible tube WEC used in this study do not exactly match those of the experimental setups. Despite these challenges, high-fidelity FSI simulations provide valuable insight into the intricate internal and external flow fields and the associated structural stress distributions of flexible tube WECs.

Building on the FSI responses of the S3 and Anaconda WECs under regular wave conditions, this section provides a comparative analysis of these flexible tube WECs. The discussion focuses on four key aspects: resonant responses, power generation, flow field characteristics, and structural responses.

A. Resonant responses

Both the S3 and Anaconda WECs rely on bulge wave generation within the flexible tube as the fundamental mechanism for wave energy conversion. However, differences in their PTO systems, such as power generation principles, spatial PTO distribution, and the number of PTO units, result in distinct resonant conditions.

The resonance of the S3 WEC is associated with the formation of standing waves inside the tube, governed by the relationship between the internal superimposed pressure wave's wavelength and the tube length, as defined by Eq. (8). Since the wavelength of the internal pressure wave varies with the external water wave, multiple standing wave modes can form within the flexible tube, as illustrated in Figs. 8 and 9. This enables the S3 WEC to achieve resonance across a broad frequency range, supporting multiple resonant frequencies.

In contrast, resonance in the Anaconda WEC is achieved when the pressure amplitude at the stern reaches its maximum, optimizing power output from the stern-located PTO. This condition requires the

stern to coincide with an anti-node of the standing wave. As demonstrated by Chaplin *et al.*,¹¹ resonance occurs when the external water wave speed matches the bulge wave velocity, which is dictated by the tube's distensibility and internal fluid density. Consequently, the Anaconda WEC typically exhibits a single dominant resonant frequency.

Moreover, our FSI simulations reveal two additional resonant frequencies for the Anaconda WEC, specifically at 0.052 and 0.65 Hz. These additional frequencies are attributed to the use of an OWC as the PTO, combined with the fixed stern and free bow boundary conditions applied to the flexible tube.

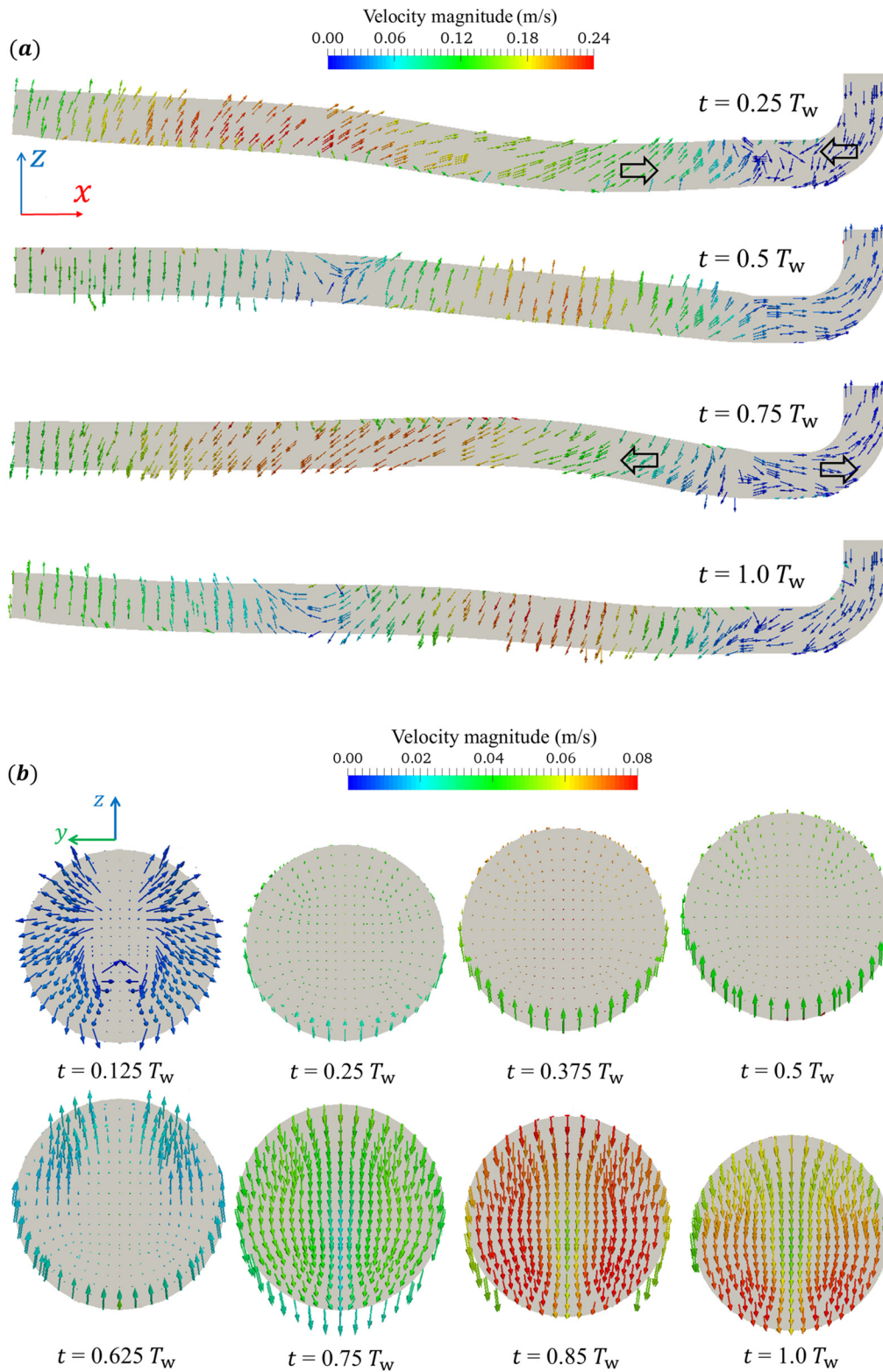
B. Power generation

Compared to the Anaconda WEC, the S3 WEC's ability to exhibit multiple resonant frequencies over a broader spectrum offers a significant advantage in power generation. This characteristic allows the S3 to achieve a higher power output capacity across a wide range of wave frequencies, enhancing its adaptability to diverse sea conditions. Moreover, the S3 employs DEG material as its PTO, which directly converts tube deformation into electrical energy, whereas the Anaconda uses a two-step process that first converts deformation into mechanical energy and then into electrical energy.

Numerical results [Figs. 17(b) and 31(a)] indicate that, for devices of equivalent size, the S3 WEC demonstrates greater power generation potential than the Anaconda WEC. It is important to note, however, that the PTO system of a flexible tube WEC is highly complex, with actual power output depending on factors, such as structural design, material properties, and control strategies. Additionally, fine-tuning the internal pressure of the tube offers a means to adjust its resonant frequency, thereby aligning it more closely with prevailing sea wave conditions and potentially enhancing overall power generation efficiency.

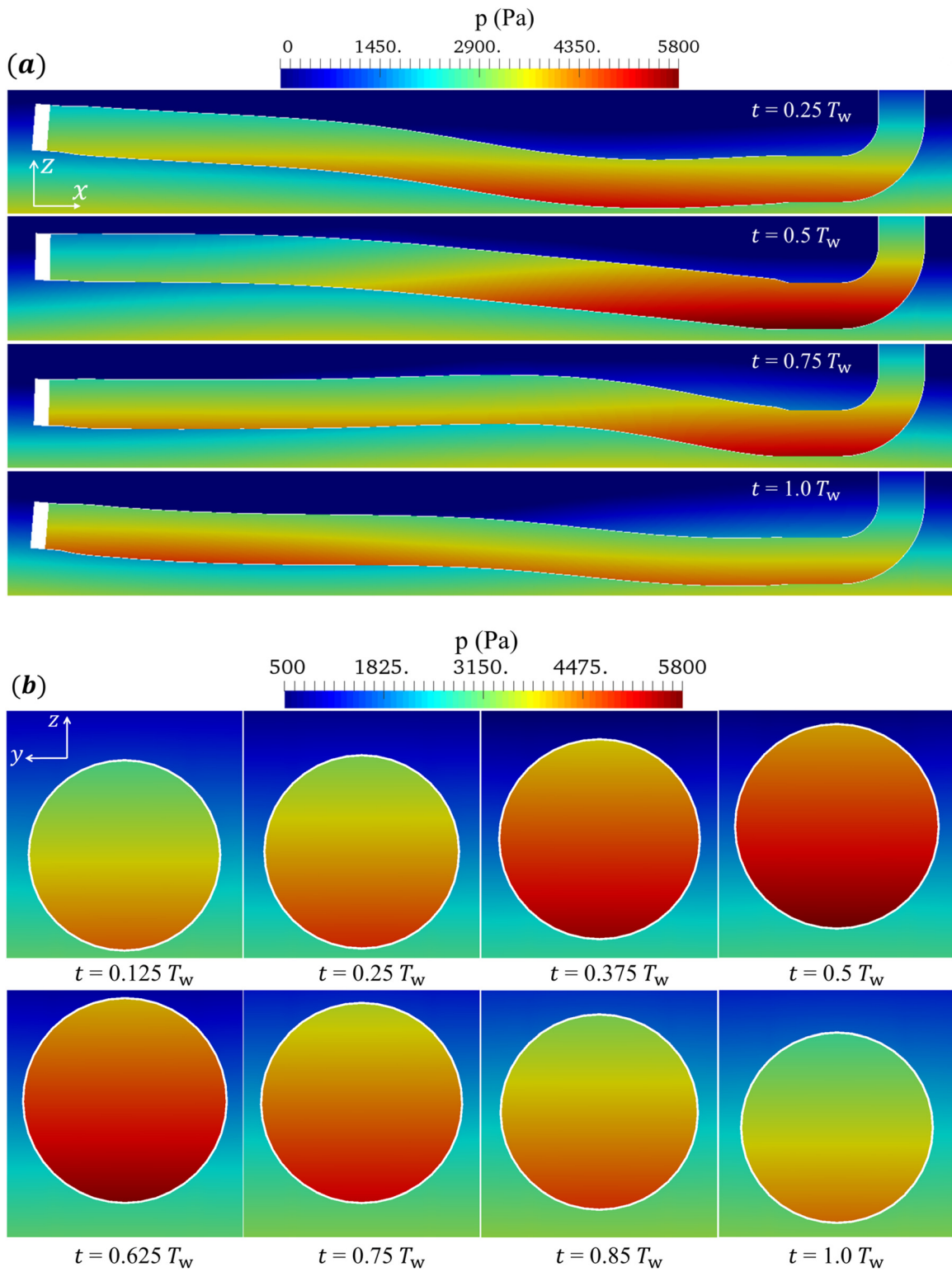
C. Flow field characteristics

The flow field of a flexible tube WEC is divided into two regions: the internal flow within the tube and the external flow surrounding it,



12 May 2025 11:42:06

FIG. 27. Velocity distribution at different sections of the Anaconda's tube at different instants within one wave period ($f_w = 0.65$ Hz): (a) $y = 0$ and (b) $x/L_1 = 0.94$.



12 May 2025 11:42:06

FIG. 28. Pressure distribution at different sections of the tube at different instants within one wave period ($f_w = 0.65$ Hz): (a) $y = 0$ and (b) $x/L_1 = 0.94$.

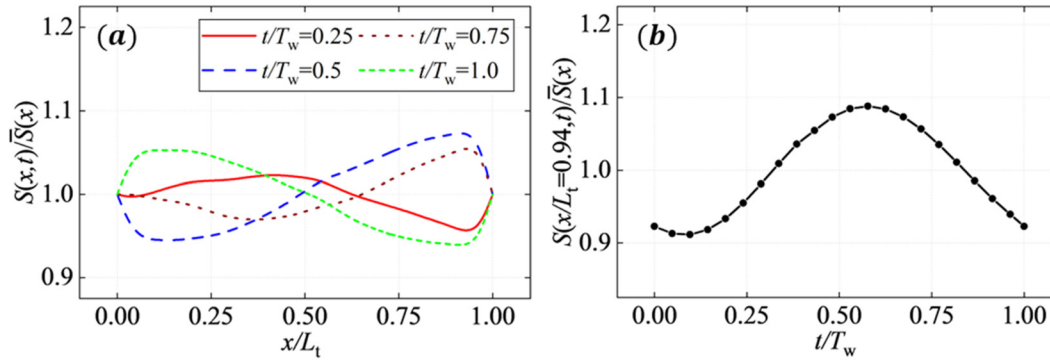


FIG. 29. Tube deformation at different instants within one wave period ($f_w = 0.65$ Hz): (a) $0 \leq x/L_t \leq 1$ and (b) $x/L_t = 0.94$.

reflecting the complex wave–structure interactions inherent in these devices. As shown in Figs. 11 and 27, the tube’s buoyancy causes it to float on the water surface, generating diffraction waves that alter both the wave elevation and the fluid forces acting on the tube. This effect has not been captured by previous reduced-order models.^{11,15,16}

In the S3 WEC, the internal flow exhibits a complex three-dimensional velocity distribution, characterized by reciprocating motion along the tube’s length and localized rotational motion at each cross section (Fig. 12). These motions are driven by the periodic deformation of the tube’s cross-sectional area and its global heave motion. In contrast, the internal flow in the Anaconda WEC primarily shows reciprocating motion along the tube, with no apparent rotational component (Fig. 27). This highlights the limitations of one-dimensional flow assumptions in reduced-order models, which fail to capture the intricate internal dynamics observed in flexible tube WECs.

Furthermore, the pressure distribution within the tube is positively correlated with its cross-sectional area and fluctuates with the tube’s expansion and contraction. Abrupt changes in velocity and flow direction at the closed ends of the tube, caused by wall boundary effects, result in significant impact loads. These loads increase the risk of structural damage to the device and underscore the importance of accurately modeling and mitigating these effects during the design process.

D. Structural responses

In flexible tube WECs, periodic deformation occurs due to pressure differences between the internal and external flow fields. This deformation, manifesting as a bulge wave, evolves over time and is influenced by external water waves, internal bulge wave reflections, pressure variations induced by tube motion, and the effects of the OWC system. Consequently, the radial deformation pattern of the tube is highly complex, resulting from the interplay of these factors.

The energy conversion mechanism in flexible tube WECs depends on how this deformation is harnessed, which varies with the type, number, and placement of PTO units. In the S3 WEC, deformation along the entire tube is used for power generation, whereas the Anaconda WEC primarily relies on deformation at the stern. As a result, the stern of the Anaconda experiences the most significant deformation and highest stress levels. In contrast, the S3 WEC exhibits

maximum deformation and stress at the anti-nodes of the internal standing waves. Since the standing wave patterns vary with external water wave frequency, the locations of peak deformation and stress shift accordingly.

VI. CONCLUSIONS

In this study, we further expanded an advanced FSI analysis framework, integrating CFD and FEA, to enable multi-physics modeling that incorporates internal fluid, external fluid, and structural fields. This enhancement allows the developed tool to be applied to a range of bio-inspired problems, such as the passive deformation of soft-bodied organisms or plants under fluid loading. We then applied this framework to investigate the dynamic behavior of two bio-inspired flexible tube WECs, e.g., the S3 WEC and the Anaconda WEC. Through a series of simulations under regular wave conditions across a range of frequencies, we conducted a comprehensive analysis of their resonant behavior, power generation efficiency, internal and external fluid field characteristics, and tube’s structural stress distributions.

The results indicate that the S3 WEC exhibits multiple standing wave modes within its tube, indicating resonant responses over a wider frequency range, whereas the Anaconda WEC demonstrates a single dominant resonant frequency. These differences in resonant behavior have a pronounced impact on power output, with the S3 WEC, equipped with distributed PTOs, achieving superior power generation. This finding underscores the potential of employing distributed PTO systems to enhance wave energy conversion efficiency. Furthermore, both devices reveal intricate internal flow dynamics that extend beyond the simplifications of one-dimensional flow assumptions. Specifically, the fluid within the S3 WEC’s tube undergoes rotational motion at each cross section, alongside reciprocating motion along the tube’s length. By contrast, the fluid motion in the Anaconda WEC is primarily characterized by reciprocating behavior, lacking rotational components. Regarding structural stress responses, the Anaconda’s peak stress is localized at the tube’s stern, whereas the S3’s maximum stress aligns with the anti-nodes of internal standing waves.

This study contributes to advancing the understanding of the FSI responses of flexible tube WECs, offering valuable insight for their design, optimization, and practical deployment. However, the scope of

12 May 2025 11:42:06

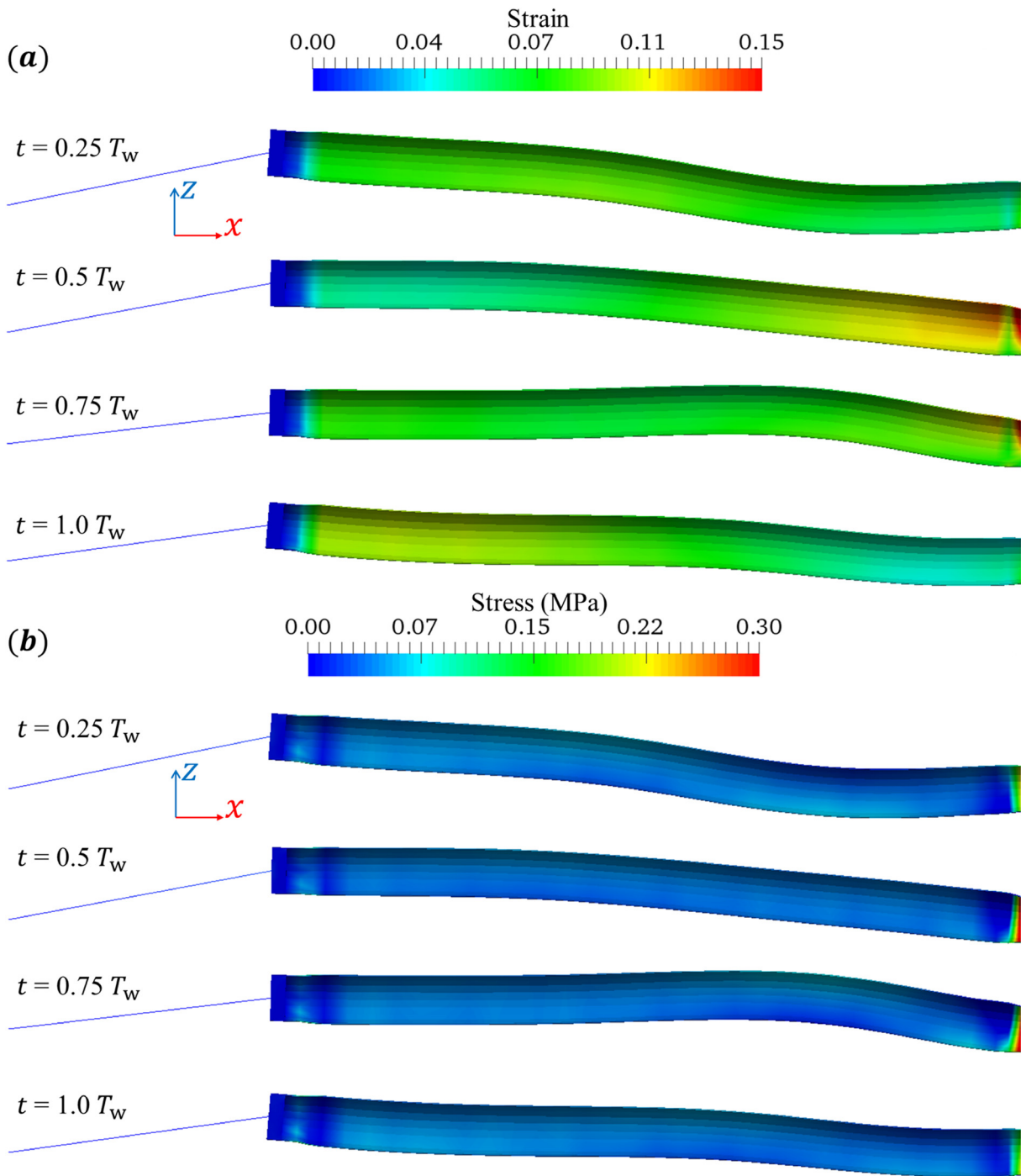


FIG. 30. Structural responses of the Anaconda WEC at different instants within one wave period ($f_w = 0.65$ Hz): (a) strain distribution and (b) stress distribution.

this work is limited by the capabilities of the current FSI tool. Specifically, the tube deformation amplitudes analyzed are modest, and scenarios involving hyper-elastic materials and irregular waves are not considered. Additionally, the effects of the electric field on material

stiffness and tube deformation in simulations of the S3 WEC with DEG PTO systems were not accounted for. These aspects will be addressed in future research to further refine the modeling and improve the applicability of the findings.

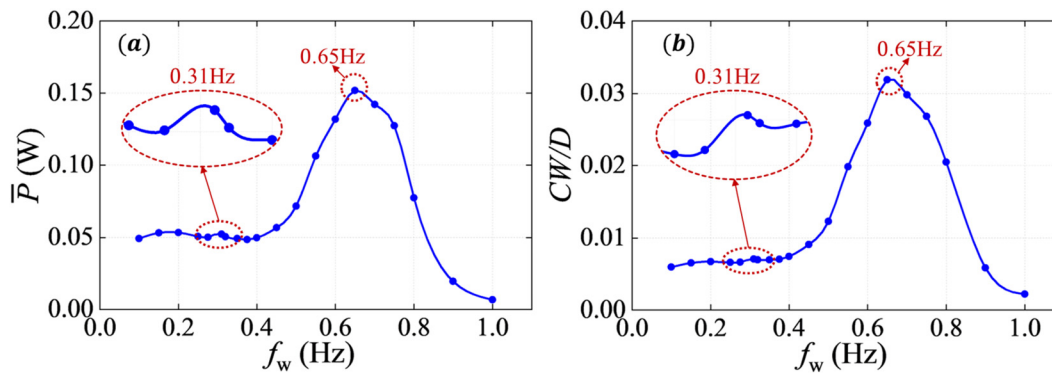


FIG. 31. Power performance of the Anaconda WEC under a series of wave frequencies: (a) time-averaged power within one wave period and (b) capture width, normalized by the tube diameter.

ACKNOWLEDGMENTS

This research was supported by an Engineering and Physical Sciences Research Council (EPSRC) Grant “Bionic Adaptive Stretchable Materials for WEC (BASM-WEC)” (EP/V040553/1). This work used the Cirrus UK National Tier-2 HPC Service at EPCC (<http://cirrus.ac.uk>) funded by the University of Edinburgh and EPSRC (EP/P020267/1).

AUTHOR DECLARATIONS

Conflict of Interest

The authors have no conflicts to disclose...

Author Contributions

Yang Huang: Conceptualization (equal); Data curation (equal); Formal analysis (equal); Investigation (equal); Methodology (equal); Software (equal); Validation (equal); Visualization (equal); Writing – original draft (equal); Writing – review & editing (equal). **Qing Xiao:** Conceptualization (equal); Formal analysis (equal); Funding acquisition (equal); Investigation (equal); Methodology (equal); Project administration (equal); Resources (equal); Software (equal); Supervision (equal); Writing – review & editing (equal). **Guillermo Idarraga:** Conceptualization (equal); Writing – review & editing (equal). **Liu Yang:** Conceptualization (equal); Funding acquisition (equal). **Saishuai Dai:** Conceptualization (equal); Formal analysis (equal); Investigation (equal); Writing – review & editing (equal). **Frahad Abad:** Conceptualization (equal); Writing – review & editing (equal). **Feargal Brennan:** Conceptualization (equal); Funding acquisition (equal). **Saeid Lotfian:** Conceptualization (equal); Formal analysis (equal); Writing – review & editing (equal).

DATA AVAILABILITY

The data that support the findings of this study are available from the corresponding author upon reasonable request.

REFERENCES

- P. Jean, A. Wates, G. Ardoise, C. Melis, R. Van Kessel, A. Fourmon, E. Barrabino, J. Heemskerck, and J. P. Queau, “Standing wave tube electro active polymer wave energy converter,” *Proc. SPIE* **8340**, 83400C (2012).
- X. Li, Q. Xiao, Y. Luo, G. Moretti, M. Fontana, and M. Righi, “Dynamic response of a novel flexible wave energy converter under regular waves,” in *The 14th European Wave and Tidal Energy Conference (EWTEC, 2021)*, pp. 1–7.
- D. Skrovanek and D. C. Ludois, “Electrostatic wave energy conversion: A review of devices, theory, and hurdles,” *IEEE Trans. Energy Convers.* **39**, 941 (2024).
- D. Golbaz, R. Asadi, E. Amini, H. Mehdipour, M. Nasiri, B. Etaati, S. T. O. Naeeni, M. Neshat, S. Mirjalili, and A. H. Gandomi, “Layout and design optimization of ocean wave energy converters: A scoping review of state-of-the-art canonical, hybrid, cooperative, and combinatorial optimization methods,” *Energy Rep.* **8**, 15446–15479 (2022).
- I. Collins, M. Hossain, W. Dettmer, and I. Masters, “Flexible membrane structures for wave energy harvesting: A review of the developments, materials and computational modelling approaches,” *Renewable Sustainable Energy Rev.* **151**, 111478 (2021).
- F. J. M. Farley and R. C. T. Rainey, *U.S. patent 7,980,071*, U.S. Patent and Trademark Office, Washington, DC (2011).
- Checkmate Flexible Engineering Ltd., 2025, see <https://www.checkmateflex.com/> (last accessed February 25, 2025).
- SBM Offshore, 2025, see <https://www.sbmoffshore.com/> (last accessed February 25, 2025).
- J. R. Chaplin, F. J. M. Farley, and R. C. T. Rainey, “Power conversion in the ANACONDA WEC,” in *Proceedings of 22nd International Workshop on Water Waves and Floating Bodies (IWWWF, 2007)*, pp. 29–32.
- V. Heller, J. R. Chaplin, F. J. M. Farley, M. R. Hann, and G. E. Hearn, “Physical model tests of the anaconda wave energy converter,” in *Proceedings of 1st IAHR European Congress*, 2010.
- J. R. Chaplin, V. Heller, F. J. M. Farley, G. E. Hearn, and R. C. T. Rainey, “Laboratory testing the Anaconda,” *Philos. Trans. R. Soc., A* **370**(1959), 403–424 (2012).
- A. C. Mendes, L. M. A. Paredes, F. A. S. Gil, and J. R. Chaplin, “Small-scale model tests of a rubber-tube wave energy converter with pneumatic power take-off,” in *International Conference on Offshore Mechanics and Arctic Engineering* (American Society of Mechanical Engineers, 2014), Vol. 45530, p. V09AT09A029.
- A. C. Mendes, F. P. Braga, L. M. A. Paredes, and J. R. Chaplin, “Performance assessment of the ANACONDA WEC in regular waves at 1: 50 model scale,” in *International Conference on Offshore Mechanics and Arctic Engineering* (American Society of Mechanical Engineers, 2017), Vol. 57786, p. V010T09A016.
- H. Yu, Z. Bai, Y. Shi, C. Zhao, X. Liu, and Y. Wang, “Hydrodynamic performance of an elastic capsule oscillating water column type WEC: An experimental study,” *Appl. Ocean Res.* **142**, 103850 (2024).
- J. R. Chaplin, F. J. M. Farley, M. E. Prentice, R. C. T. Rainey, S. J. Rimmer, and A. T. Roach, “Development of the ANACONDA all-rubber WEC,” in *7th European Wave and Tidal energy Conference*, 2007.

- ¹⁶F. J. M. Farley, R. C. T. Rainey, and J. R. Chaplin, "Rubber tubes in the sea," *Philos. Trans. R Soc. A* **370**(1959), 381–402 (2012).
- ¹⁷A. Babarit, J. Singh, C. Mélis, A. Watez, and P. Jean, "A linear numerical model for analysing the hydroelastic response of a flexible electroactive wave energy converter," *J. Fluids Struct.* **74**, 356–384 (2017).
- ¹⁸A. King, C. Algie, S. Ryan, and R. Ong, "Modelling of fluid structure interactions in submerged flexible membranes for the Bombora wave energy converter," in 20th Australasian Fluid Mechanics Conference, Perth, Australia, 2016.
- ¹⁹S. Zou and O. Abdelkhalik, "A numerical simulation of a variable-shape buoy wave energy converter," *J. Mar. Sci. Eng.* **9**(6), 625 (2021).
- ²⁰M. A. Shabara, S. Zou, and O. Abdelkhalik, "Numerical investigation of a variable-shape buoy wave energy converter," in *International Conference on Offshore Mechanics and Arctic Engineering* (American Society of Mechanical Engineers, 2021), Vol. 85192, p. V009T09A013.
- ²¹F. N. Van de Vosse and N. Stergiopoulos, "Pulse wave propagation in the arterial tree," *Annu. Rev. Fluid Mech.* **43**, 467–499 (2011).
- ²²K. F. Graff, *Wave Motion in Elastic Solids* (Clarendon Press, Oxford, UK, 2012).
- ²³T. J. Pedley, *The Fluid Mechanics of Large Blood Vessels* (Cambridge University Press, Cambridge, MA, 1980).
- ²⁴J. H. Gerrard, "An experimental test of the theory of waves in fluid-filled deformable tubes," *J. Fluid Mech.* **156**, 321–347 (1985).
- ²⁵J. B. A. M. Horsten, A. A. Van Steenhoven, and M. E. H. Van Dongen, "Linear propagation of pulsatile waves in viscoelastic tubes," *J. Biomech.* **22**(5), 477–484 (1989).
- ²⁶J. K. Li, J. Melbin, R. A. Riffle, and A. Noordergraaf, "Pulse wave propagation," *Circ. Res.* **49**(2), 442–452 (1981).
- ²⁷Bionic Adaptive Stretchable Materials for Wave Energy Converters Project, 2025, see <https://gtr.ukri.org/projects?ref=EP%2FV040553%2F1> (last accessed February 25, 2025).
- ²⁸F. Abad, S. Lotfian, S. Dai, G. Zhao, G. I. Alarcon, L. Yang, Y. Huang, Q. Xiao, and F. Brennan, "Experimental and computational analysis of elastomer membranes used in oscillating water column WECs," *Renewable Energy* **226**, 120422 (2024).
- ²⁹G. Idarraga, L. Yang, F. Abad, Y. Huang, S. Dai, Q. Xiao, S. Lotfian, and F. Brennan, "Hyperelastic behaviour of elastomers for wave energy applications," *Ocean Eng.* **313**, 119652 (2024).
- ³⁰Y. Huang, Q. Xiao, G. Idarraga, L. Yang, S. Dai, F. Abad, F. Brennan, and S. Lotfian, "Novel computational fluid dynamics-finite element analysis solution for the study of flexible material wave energy converters," *Phys. Fluids* **35**(8), 083611 (2023).
- ³¹Y. Huang, Q. Xiao, G. Idarraga, L. Yang, S. Dai, F. Abad, F. Brennan, and S. Lotfian, "Numerical analysis of flexible tube wave energy converter using CFD-FEA method," in *Proceedings of the ASME 2023 42nd International Conference on Ocean, Offshore and Arctic Engineering* (ASME, 2023), p. 101302.
- ³²Y. Huang, G. Idarraga, F. Abad, Q. Xiao, L. Yang, S. Dai, S. Lotfian, and F. Brennan, "Oscillating water column wave energy converter with flexible structured sheet material for enhanced power output," *Energy Convers. Manage.* **333**, 119794 (2025).
- ³³P. Higuera, J. L. Lara, and I. J. Losada, "Three-dimensional interaction of waves and porous coastal structures using OpenFOAM®. Part I: Formulation and validation," *Coastal Eng.* **83**, 243–258 (2014).
- ³⁴P. Higuera, J. L. Lara, and I. J. Losada, "Three-dimensional interaction of waves and porous coastal structures using OpenFOAM®. Part II: Application," *Coastal Eng.* **83**, 259–270 (2014).
- ³⁵G. Dhondt, *Calculix Crunchix User's Manual Version 2.12*, Munich, Germany, 2017 (last accessed September 21, 2017).
- ³⁶H. J. Bungartz, F. Lindner, B. Gatzhammer, M. Mehl, K. Scheufele, A. Shukaev, and B. Uekermann, "preCICE—A fully parallel library for multi-physics surface coupling," *Comput. Fluids* **141**, 250–258 (2016).
- ³⁷F. Lindner, M. Mehl, and B. Uekermann, "Radial basis function interpolation for black-box multi-physics simulations," in VII International Conference on Computational Methods for Coupled Problems in Science and Engineering, 2017.
- ³⁸J. Degroote, K. J. Bathe, and J. Vierendeels, "Performance of a new partitioned procedure versus a monolithic procedure in fluid–structure interaction," *Comput. Struct.* **87**(11–12), 793–801 (2009).
- ³⁹G. Idarraga, L. Yang, F. Abad, Y. Huang, S. Dai, Q. Xiao, S. Lotfian, and F. Brennan, "Hyperelastic modelling of elastomers for wave energy converters," in *International Conference on Offshore Mechanics and Arctic Engineering* (American Society of Mechanical Engineers, 2023), Vol. 86854, p. V003T03A001.
- ⁴⁰X. Li and Q. Xiao, "A numerical study on an oscillating water column wave energy converter with hyper-elastic material," *Energies* **15**(22), 8345 (2022).
- ⁴¹K. L. Gee, "The Rubens tubes," *Proc. Meet. Acoust.* **8**(1), 025003 (2009).
- ⁴²G. Moretti, G. P. R. Papini, L. Daniele, D. Forehand, D. Ingram, R. Vertechy, and M. Fontana, "Modelling and testing of a wave energy converter based on dielectric elastomer generators," *Proc. R. Soc. A* **475**(2222), 20180566 (2019).
- ⁴³R. D. Barree and M. W. Conway, (2004, September). "Beyond beta factors: A complete model for Darcy, Forchheimer, and trans-Forchheimer flow in porous media," in *SPE Annual Technical Conference and Exhibition* (OnePetro, 2004), Paper No. SPE-89325-MS.
- ⁴⁴J. Lighthill, *Waves in Fluids* (Cambridge University Press, Cambridge, UK, 2001).
- ⁴⁵J. F. Toland, *Stokes Waves* (Juliusz Schauder Center for Nonlinear Studies, 1996).